2015

Dust, Volcanic Ash, and the Evolution of the South Pacific Gyre through the Cenozoic

Ann G. Dunlea

Richard W. Murray

See next page for additional authors

Citation/Publisher Attribution

Dunlea, A. G., Murray, R. W., Sauvage,J., Spivack, A. J., D'Hondt, S., & Harris, R. N. (2015). Dust, volcanic ash, and the evolution of the South Pacific Gyre through the Cenozoic. *Paleoceanography, 30* (8), 1078-1099.
Available at: http://dx.doi.org/10.1002/2015PA002829

AGU PUBLICATIONS

Paleoceanography

RESEARCH ARTICLE
10.1002/2015PA002829

Key Points:
- Forty-seven element concentrations in 206 bulk sediment samples from seven sites in the South Pacific
- Multivariate statistical models quantify dust, ash, and other fluxes 100–0 Ma
- Dust and ash records climate and meridional shifts in atmospheric circulation

Supporting Information:
- Readme
- Figure S1
- Table S1
- Table S2
- Table S3
- Table S4
- Table S5

Correspondence to:
A. G. Dunlea,
adunlea@bu.edu

Citation:
Dunlea, A. G., R. W. Murray, J. Sauvage, A. J. Spivack, R. N. Harris, and S. D'Hondt (2015), Dust, volcanic ash, and the evolution of the South Pacific Gyre through the Cenozoic, *Paleoceanography*, *30*, doi:10.1002/2015PA002829.

Received 5 MAY 2015
Accepted 7 JUL 2015
Accepted article online 14 JUL 2015

Dust, volcanic ash, and the evolution of the South Pacific Gyre through the Cenozoic

Ann G. Dunlea[1], Richard W. Murray[1], Justine Sauvage[2], Arthur J. Spivack[2], Robert N. Harris[3], and Steven D'Hondt[2]

[1]Department of Earth and Environment, Boston University, Boston, Massachusetts, USA, [2]Graduate School of Oceanography, University of Rhode Island, Narragansett, Rhode Island, USA, [3]College of Earth, Ocean, and Atmospheric Sciences, Oregon State University, Corvallis, Oregon, USA

Abstract We examine the 0–100 Ma paleoceanographic record retained in pelagic clay from the South Pacific Gyre (SPG) by analyzing 47 major, trace, and rare earth elements in bulk sediment in 206 samples from seven sites drilled during Integrated Ocean Drilling Program Expedition 329. We use multivariate statistical analyses (Q-mode factor analysis and multiple linear regression) of the geochemical data to construct a model of bulk pelagic clay composition and mass accumulation rates (MAR) of six end-members, (post-Archean average Australian shale, rhyolite, basalt, Fe-Mn-oxyhydroxides, apatite, and excess Si). Integrating the results with Co-based age models at Sites U1365, U1366, U1369, and U1370, we link changes in MAR of these components to global oceanographic, terrestrial, and climatic transformations through the Cenozoic. Our results track the spatial extent (thousands of kilometers) of dust deposition in the SPG during the aridification of Australia. Dispersed ash is a significant component of the pelagic clay, often comprising >50% by mass, and records episodes of Southern Hemisphere volcanism. Because both are transported by wind, the correlation of dust and ash MAR depends on the site's latitude and suggests meridional shifts in the position of atmospheric circulation cells. The hydrothermal MARs provide evidence for rapid deposition from the Osbourn Trough spreading ridge before it went extinct. Excess Si MARs show that the abrupt increase in siliceous productivity observed at Site U1371 also extended at least as far north as Sites U1369 and U1370, suggesting large-scale reorganizations of oceanic Si distributions ~10–8 Ma in the southern SPG.

1. Introduction

Understanding provenance and accumulation rates of pelagic clay in the South Pacific Gyre (SPG) provides insight into major paleoceanographic and paleoclimatic events [e.g., *Zhou and Kyte*, 1992; *Rea et al*., 2006; *Stancin et al*., 2008]. However, identification of provenance is complicated by authigenic processes that alter the mineralogy and chemical composition of the primary source of sediment. Authigenic phases found in the SPG such as Fe-Mn oxyhydroxides or Mn-enriched nodules (or hardgrounds) can concentrate Th, rare earth elements (REEs), and other elements, limiting the use of these and other commonly employed geochemical tracers [e.g., *Li and Schoonmaker*, 2003].

Another challenge to understanding SPG clay provenance is differentiating aluminosilicate eolian dust from aluminosilicate volcanic ash produced by the abundant subduction-zone volcanism surrounding the SPG. Ash layers are present in the pelagic sediment at all the sites drilled during Integrated Ocean Drilling Program (IODP) Expedition 329, except at the youngest Site U1368 [*D'Hondt et al*., 2011]. In addition to these discrete ash layers, much ash is mixed into the bulk sediment as "dispersed" ash, which can be invisible to the naked eye but still be chemically detectable, although it may be somewhat altered [*Yamamoto et al*., 1986; *Peters et al*., 2000; *Scudder et al*., 2009, 2014]. Differentiating the dispersed ash (including both altered- and unaltered ash materials) from other terrigenous sediments is important in order to develop an accurate record of nonvolcanic terrigenous inputs.

To distinguish subtle differences in provenance, we apply a variety of discrimination techniques to the chemical compositional data of bulk SPG sediment samples collected during IODP Expedition 329. Although we interpret the geochemistry of different lithologies from all seven sites to identify basin-wide spatial patterns of sediment provenance, in this study we mainly focus on the pelagic *clay* intervals present at each of the Expedition 329 sites except Site U1368. We statistically model chemical compositional data of bulk SPG pelagic clay to identify and quantify end-member components. By applying Co-based age models constructed for the four sites

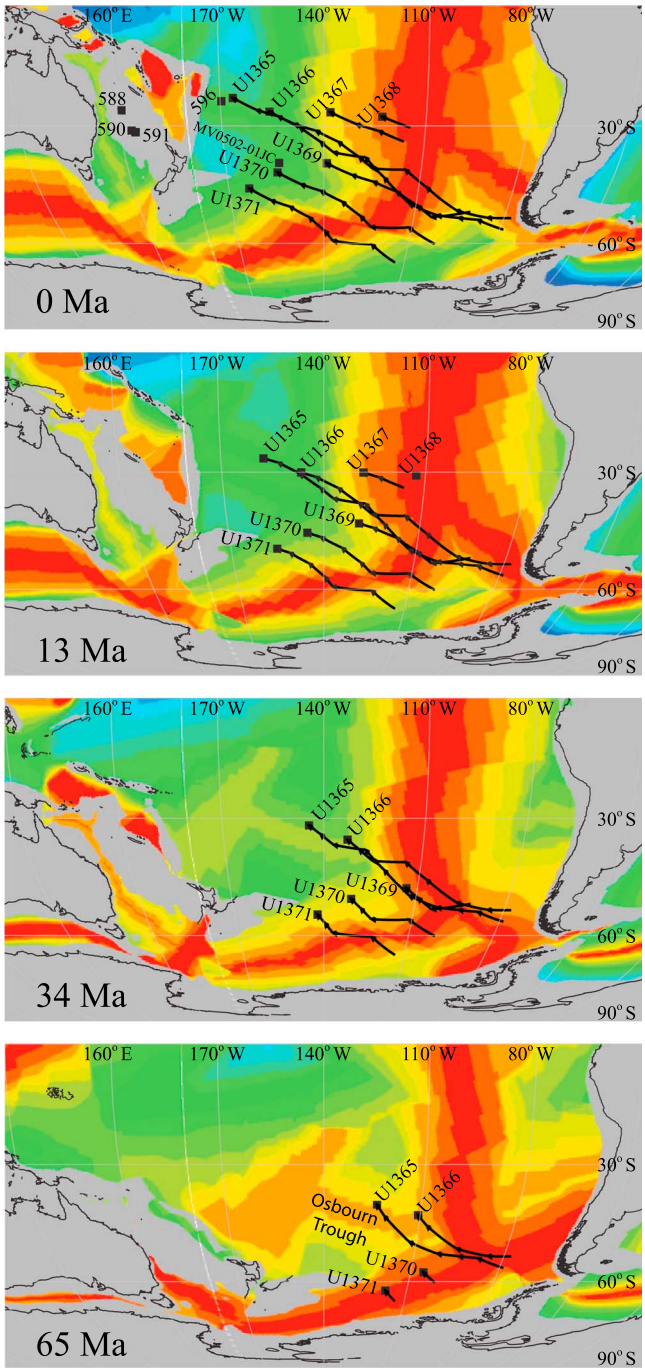

Figure 1. Backtrack paths of the seven sites drilled during IODP Expedition 329 plotted on a background map of the age of the oceanic lithosphere at various times through the Cenozoic. Each tick along the backtrack paths denotes a 10 Myr increment. Core MV0502-01JC and Deep Sea Drilling Project (DSDP) Sites 588, 590, 591, and 596 are plotted for reference. Maps were generated using GPlates open source software and plate reconstructions [*Seton et al.*, 2012; *Gurnis et al.*, 2012]. Paths are plotted against a latitude/longitude reference frame and thus appear to cross the East Pacific Rise when in reality each site's history has entirely been on the Pacific Plate.

predominantly composed of pelagic clay (Sites U1365, U1366, U1369, and U1370) [*Dunlea et al.*, 2015], we determine mass accumulation rates of the sedimentary components and identify when changes in provenance and accumulation rates occurred over the past ~60–100 Ma, depending on the age of each site. We interpret changes in the sedimentary mass accumulation rates and composition in the context of various regional and global events. Combining provenance information from this study with the few other sedimentary records in the South Pacific, we present an unprecedented spatially and temporally extensive paleoceanographic history of the SPG from the beginning of the Cenozoic to the modern.

2. Pelagic Clay Lithology

Seven sites were drilled during Expedition 329 (Figure 1). Except for Site U1371, the pore fluids at each site are oxic through the entire sediment section [*D'Hondt et al.*, 2015] and there is no evidence that the sites were anoxic in the past. The predominant sediment lithology throughout the Expedition 329 sites is a fine-grained, homogenous, brown pelagic clay [*D'Hondt et al.*, 2011]. In addition to the pelagic clay, siliceous deposits exist at Site U1371 (0–104 meters below seafloor, mbsf), at Site U1365 as chert (from ~ 44 to 62 m below seafloor, mbsf), and as thin porcellanite layers interlaced with the pelagic clay at Sites U1365 and U1366. Calcareous deposits are preserved at the younger, shallower Sites U1367 and U1368 and at the deeper Site U1370 as a thin layer of nannofossil ooze at ~62 mbsf. Additional minor lithologies include multiple discrete ash layers, and at least two types of altered ashes were reported at Site U1366 based on color alone. There is visible dispersed volcanic glass in smear slides throughout the entire sediment

column at Sites U1365, U1366, and U1370. Other significant phases within the pelagic clay are red semiopaque oxides and zeolites [*D'Hondt et al*., 2011].

To obtain relatively complete records at Sites U1365, U1366, and U1370 we use samples taken from different holes at each site. Stratigraphic correlation with a high degree of confidence between holes at these sites is difficult, because a high number of whole-round samples were taken for microbiology and geochemistry prior to collecting the multisensor track (MST) and natural gamma radiation (NGR) data and there is low variability in the NGR and MST records of the remaining sediment.

Apart from the lithostratigraphy, there is no formal stratigraphic correlation between holes [*D'Hondt et al*., 2011]. For Site U1366, we modified the originally published depths to align distinct features and trends in the MST and NGR data as well as trends in our geochemical data set. The modified depths improve the correlation between holes at Site U1366 in each data set and are reported along with the original depths (Table S1 in the supporting information). At Sites U1365, U1369, and U1370, the patchy MST, NGR, and geochemical data from multiple holes suggest that the holes are approximately aligned but are insufficient to confidently refine further. Thus, we use the published depths at these sites [*D'Hondt et al*., 2011].

3. Analytical Procedures

Most of our bulk sediment samples are from 10 cm long whole-round cores (Table S1) that are nominally evenly spaced by depth at each site and had pore fluids extracted via squeezing in a hydraulic press [*D'Hondt et al*., 2011]. Additionally, we analyzed 20 discrete samples taken with plastic plugs to fill gaps or to sample material that was visually identified as being ash or other specific lithologies (Table S2).

We conducted all additional sample preparation and analysis in the Analytical Geochemistry Facilities at Boston University. Reagents used for sediment digestion were either UltraPure grade (Fisher, New Jersey) or double distilled at Boston University. MilliQ water (18.2 MΩ) was used for dilutions.

We freeze-dried a representative subsample of each sample and hand powdered it in an agate mortar and pestle. For major element analyses, we dissolved samples by flux fusion broadly following techniques described by *Murray et al*. [2000]. In detail, we combined 100 ± 0.5 mg of sample powder with 400 ± 0.5 mg of lithium metaborate ($LiBO_2$) in an ultrapure graphite crucible and heated the mixture at 1050°C for 10 min. We directly poured the resulting molten mixture into 50 mL of 5% nitric acid, sonicated the fluid, filtered it through a 0.45 μm Millex filter unit fitted to an 12 mL high-density polyethylene plastic syringe, and rediluted it to a final dilution factor of 1:4000 by mass. During dissolution, samples were manually shaken (not stirred). We analyzed the solutions by inductively coupled plasma emission spectrometry (ICP-ES) for all 10 major elements, as well as Sc, V, Cr, Ni, Cu, Zn, Sr, Y, Zr, and Ba (Tables S1 and S2).

For the analysis of additional trace elements and REEs, we weighed 20 ± 2 mg of sample powder into a Teflon™ vial to which we added 2 mL of HNO_3, 1 mL of HCl, and 1 mL of HF. We then sealed the vial and heated it on a hot plate at subboiling temperature for ~24 h. After sonicating for 60 min, we added 1 mL of H_2O_2, resealed the vials, and heated them on the hotplate overnight. We then dried the samples and redissolved them in 1 mL of HNO_3 and 0.5 mL of H_2O_2. We diluted these solutions to 60 g (3000 times dilution) with 18.2 MΩ H_2O and analyzed them by inductively coupled plasma mass spectrometry (ICP-MS) (Tables S1 and S2).

For both ICP-ES and ICP-MS analyses, we analyzed three separate digestions of a homogenized SPG sediment in-house standard with each batch to quantify precision (standard deviation/average * 100), which we determined to be ~2% for each element. We prepared and analyzed the international Standard Reference Material, BHVO-2, as an unknown with each batch run on the ICP-ES and ICP-MS. Our measured concentrations for BHVO-2 were compared to the known element concentrations and were consistently found to be accurate within precision throughout the element menu.

4. Multivariate Statistical Techniques

We computed multivariate statistics using MATLAB™ algorithms tailored for geochemical mixing problems [*Pisias et al*., 2013]. These algorithms have been successfully applied by our research group to samples from a diverse range of other ocean regions [e.g., *Ziegler and Murray*, 2007; *Ziegler et al*., 2007, 2008;

Scudder et al., 2009, 2014; *Martinez et al*., 2009, 2010]. Variations of these codes have also been used by other research groups over the past decades (as described in *Pisias et al*. [2013]).

Q-mode Factor Analysis (QFA) is an exploratory statistical technique used to identify elements that covary in a data set and to determine the minimum number of components needed to explain a given fraction of the variance of the data set [*Pisias et al*., 2013, and references therein]. Prior to performing factor analysis, we pretreated the data set by normalizing each element concentration to the concentration range of that element. During QFA, elements that covary in the data set were grouped into "factors" and a VARIMAX rotation was applied to keep the factors orthogonal to one another while maximizing the variance explained by each of the factors. Each VARIMAX-rotated factor indicates a unique sediment source, and the elements that covary strongly within that factor can provide clues as to the type of sediment source that factor represents. Elements that covary strongly within a factor will have high-absolute value VARIMAX factor *scores* in that factor. The importance of each factor to the variability of each sample is recorded by the VARIMAX factor *loadings* value, which can help reveal patterns in the importance of each factor throughout a sediment column or between different sites.

While QFA allows us to identify the number and general categories of end-members in the bulk sediment, a constrained least squares (CLS) multiple linear regression model is required to quantify the proportion (and eventually the mass accumulation rate) of each end-member in each sample [*Pisias et al*., 2013, and references therein]. For the CLS model, we input geologically reasonable end-member compositions from the literature and discrete ash layer compositions analyzed in this study that corresponded to each of the factors suggested by the QFA results. The CLS mixing model then determines the optimal proportions of each end-member ($\geq$ zero) that combine to form the composition of each bulk sediment sample. This algorithm minimizes the sum of the squared residuals between the CLS model and the given data set. Goodness-of-fit of a CLS model to the given data set is measured by two statistical parameters: the coefficients of determination (an R^2 value for each element) and the fraction (percent) of the compositional data explained by the model. We used these two parameters to identify the end-members that best explain the data set, as discussed in more detail in the later sections regarding end-member selection in the context of geological reasonableness.

5. Bulk Pelagic Clay Characterization

Throughout this study, we focus our partitioning techniques on the pelagic clay lithology common throughout the Expedition 329 sites to assess basin-wide changes of provenance throughout deep time. Previous work on deep-sea homogenous pelagic clay [e.g., *Leinen*, 1987; *Zhou and Kyte*, 1992; *Kyte et al*., 1993] demonstrates that this material is a complex mixture of aluminosilicate debris (from eolian sources, altered basalt, etc.), hydrothermal inputs (most commonly, but not exclusively, found directly overlying the basement rock), biogenic material (including apatite fish debris), and other inputs. Superimposed on these sources are the effects of authigenic processes, which modify previously existing phases and/or create entirely new phases on and in the seafloor [e.g., *Kastner*, 1999; *Cuadros et al*., 2011]. In light of these sources and authigenic processes, we explore the origin of SPG pelagic clay through a variety of partitioning techniques applied to the geochemical compositions of the samples. In this section 5, we examine key major and trace element patterns from the pelagic clay intervals from Sites U1365, U1366, U1369, and U1370 to provide a first-order assessment of the main components of SPG pelagic clay to guide later statistical partitioning described in section 6.

5.1. Bulk Pelagic Clay Characterization: Bulk Chemical Composition

5.1.1. Fe-Mn Oxyhydroxide Component

Hydrothermal vents emit dissolved Fe, Mn, Zn, and other elements into the water column [e.g., *Elderfield and Schultz*, 1996]. Rapid removal of these elements when the hydrothermal fluid mixes with ambient ocean water causes elevated Fe-Mn oxyhydroxide deposition near mid-ocean ridges (MOR). Reflected by high Fe/Al and Zn/Al ratios (Figures 2a and 2b), deposition from hydrothermal vents and plumes is highest directly above the basement rock and decreases rapidly upsection. This enrichment in Fe and Zn in the SPG sediment coincides with higher abundances of red semiopaque oxides [*D'Hondt et al*., 2011].

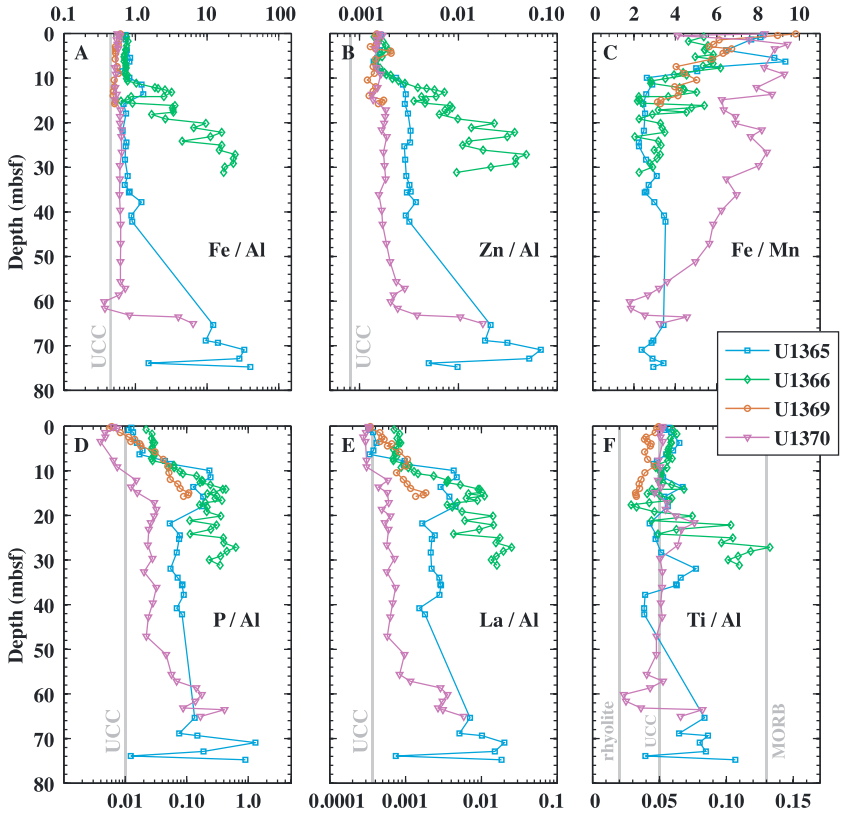

Figure 2. (a–f) Element ratio (g/g) depth profiles for the four sites dominated by pelagic clay. The grey vertical lines in some subplots depict average values for upper continental crust (UCC) [*Rudnick and Gao*, 2003], rhyolite (Geochemistry of Rocks of the Oceans and Continents (GEOROC), 2014, http://georoc.mpch-mainz.gwdg.de/georoc/) and mid-ocean ridge basalt (MORB) [*Gale et al.*, 2013], as labeled. Note the different scales on the *x* axes.

Dissolved hydrothermal Fe and Mn can be advected horizontally in the water column for thousands of kilometers [*Saito et al.*, 2013; *Fitzsimmons et al.*, 2014]. As hydrothermal plumes spread, these elements continue to be deposited at the seafloor causing the Fe/Al and Zn/Al ratio (Figures 2a and 2b) of younger sediment deposited farther from the MOR to remain higher than the average continental values of Fe/Al (~0.43 g/g) and Zn/Al (~0.00082 g/g) [*Rudnick and Gao*, 2003].

As the amount of hydrothermal deposition (Fe/Al) decreases as a site moves away from the MOR, the Fe/Mn ratio increases (Figure 2c) showing the increasing relative importance of Fe deposition farther from the ridge. Fe and Mn deposited far from the MOR may adsorb to or precipitate on preexisting aluminosilicates, be incorporated in authigenic minerals, or as part of Fe-Mn oxyhydroxide nodules/micronodules and crusts within or on the sediment.

5.1.2. Apatite and Authigenic Enrichments

Apatite from fish debris (e.g., teeth and bones) is concentrated in slowly accumulating open ocean sediment deposited below the calcite compensation depth. Since P is a structural component of apatite and apatite is the dominant source of P in pelagic clay [e.g., *Li and Schoonmaker*, 2003], the upsection decrease of P/Al ratio at each SPG site (Figure 2d) may broadly indicate an increase in sedimentation rate as each site migrated from the center of the South Pacific toward continents (Figure 1). Shallower sediment approaches continental P/Al values (~0.01 g/g) [*Rudnick and Gao*, 2003] at each site (Figure 2d), suggesting continental material (i.e., dust) becomes a more important influence on the P/Al in these intervals. Phosphorus also adsorbs onto and/or coprecipitates with Fe-Mn oxyhydroxides [e.g., *Lyle*, 1986; *Marchig and Erzinger*, 1986; *Wheat et al.*, 1996] that may influence parts of the P/Al profile.

Fish debris deposited in marine sediment with a long seawater exposure time [e.g., *Ruhlin and Owen*, 1986] incorporates REEs and certain other trace elements into the apatite structure [e.g., *Takebe*, 2005]. This enrichment of REEs (La/Al, Figure 2e) dominates the REE abundances and patterns in the bulk sediment

and inhibits the use of particular aluminosilicate discrimination indicators (e.g., La-Th-Sc) that are commonly employed to distinguish provenance [e.g., *Ziegler et al*., 2007].

5.1.3. Aluminosilicate Input

At least two, and possibly three, aluminosilicate end-members are indicated by the Ti/Al ratio, a ratio minimally affected by authigenesis and/or diagenesis [*Yamamoto et al*., 1986; *Li and Schoonmaker*, 2003]. Downhole profiles show ranges of high to low Ti/Al ratios (0.13–0.02 g/g) throughout Sites U1365, U1366, U1369, and U1370 (Figure 2f). Altered basaltic grains in the sediment are present near the basement [*D'Hondt et al*., 2011], which could explain the high Ti/Al near the base at Sites U1365, U1366, and U1370. Multiple discrete ash layers within the sediment have a rhyolitic Ti/Al (0.02 g/g) (GEOROC, online report, 2014) and therefore, dispersed ash may be carrying the low Ti/Al signature. Because the Ti/Al ratio is unaffected by ash alteration, it does not discriminate between altered versus unaltered ash material but instead detects variations in the original ash composition. Further upsection, near the seafloor, Ti/Al ratios at each site approach an intermediate value (~0.05 g/g), indicating either a mixture of the high Ti/Al and low Ti/Al sources or the presence of a third intermediate source such as post-Archaean Australian shale (PAAS) (0.06 g/g) [*Taylor and McLennan*, 1985] or Upper Continental Crust (0.05 g/g) [*Rudnick and Gao*, 2003].

5.2. Bulk Pelagic Clay Characterization: QFA

The QFA and subsequent CLS modeling was performed on the pelagic clay samples (sample size, $n = 138$) from Sites U1365, U1366, U1367, U1369, U1370, and U1371 (excluding the samples of calcareous and siliceous lithology from Sites U1367 and U1371, respectively). The initial QFA was run with a broad and inclusive element menu, in order to capture the maximum number of potential sources and processes. This approach does not assume that any given element is specifically associated with a particular end-member component or exclusively from a single source. The element menu consisted of nine major elements (Si, Al, Ti, Fe, Mn, Ca, Mg, K, and P, excluding Na because it is predominantly from sea salt) and 13 trace elements (Sc, V, Cr, Co, Cu, Zn, Rb, Zr, Nb, Cs, La, Hf, and Th).

The QFA indicates that four factors explain 96% of the variance (Figure 3 and Table S3). Factor 1 explains 56% of the variance and indicates that Si, Al, Ti, K, Cr, Rb, and Cs covary strongly. The presence of Al, Ti, and Cr in Factor 1 suggests that it represents an aluminosilicate. Fe, Mn, Mg, V, Cu, and Zn covary in a second factor that explains 20% of the variance and that we interpret to represent an Fe-Mn oxyhydroxide phase(s) associated with hydrothermal/hydrogenous oxide deposits and/or oxide coatings on preexisting deposits. Factor 3 explains 16% of the variance and has high-factor scores for Ca, P, Sc, Co, Zr, Nb, La, and Hf, which we interpret to represent biogenic carbonate fluorapatite (CFA) enriched in REEs and/or elements scavenged by oxides during periods of slow sedimentation. The fourth factor explains 4% of the variability of the data set and isolates Si. We interpret this factor to represent excess Si from biogenic opal and/or a Si-enriched authigenic phase [e.g., *Dymond and Eklund*, 1978].

We ran multiple tests to check the statistical stability of our modeling and ensure that the identification and composition of these four factors are not sensitive to the particular element menu used or to any of the statistical parameterizations. Even though the number of elements in the menu is greater than the 17-element maximum recommended by *Reimann et al*. [2002] for the number of samples we used, similar factors were generated when the element menu was progressively decreased to as few as six elements. For example, a QFA run with Al, Ti, Fe, Zn, and Hf explained 98% of the variability of the data set with three factors that corresponded to aluminosilicate (Al and Ti), Fe-Mn oxyhydroxide (Fe and Zn), and authigenically enriched (Hf) components.

We conducted other tests to confirm the factors are robust. For example, if we excluded Si from the element menu, only the first three factors were identified. Also, because the sample size at each site varies (from 18 at Site U1369 to 45 at Site U1366), we ran model iterations to assess whether one site influenced the results of all the six sites combined. We chose 18 samples approximately evenly spaced by depth from each of the four sites dominated by pelagic clays (Sites U1365, U1366, U1369, and U1370) to ensure that each site was equally represented in the data set. For this test, we excluded the five most biogenic Si-enriched samples to avoid skewing the results. The QFA of the combined sites ($n = 72$) with the 22-element menu produced nearly identical factors and factor loadings to the first three factors of the complete sample data set. Therefore, we conclude that one site is not biasing the results for the whole data set.

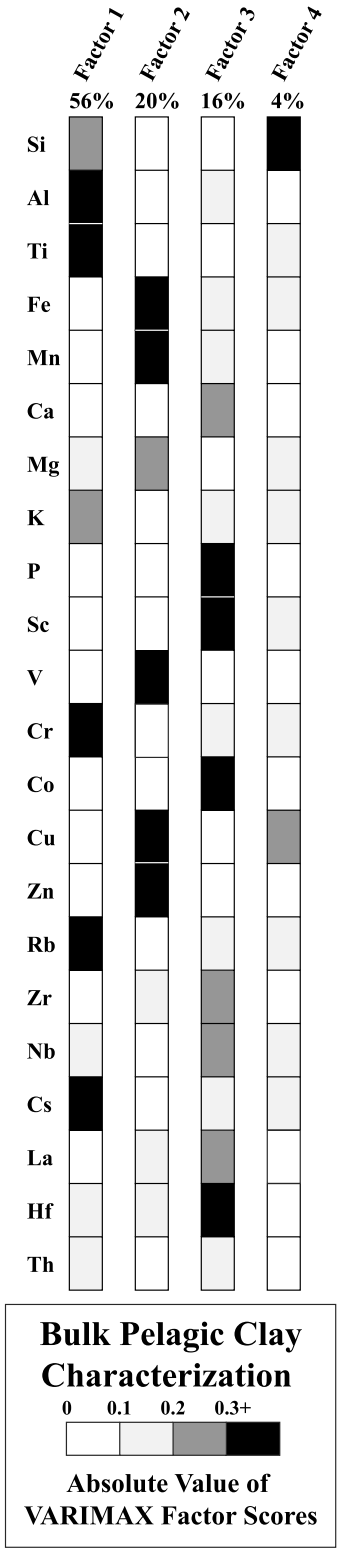

Figure 3. Factors 1, 2, 3, and 4 from the 22-element QFA run with 138 pelagic clay samples. The % variability of the data set explained by each factor is reported at the top of each column. Each row is an element used in the QFA, and the color in the boxes corresponds to the absolute value of the VARIMAX-rotated factor scores of each element in each factor. The darker the color, the stronger those elements covary within each factor.

For another test, we excluded all of the elements with high-factor scores in Factor 1 (that is, Al, Ti, K, Cr, Rb, and Cs) from the 22-element QFA. This new 14-element QFA shows that Nb, Hf, and Th covary with Factor 1 and produced factor loading patterns that are nearly identical to the first factor in the 22-element QFA. This test indicates that Nb, Hf, and Th are partly associated with the aluminosilicate factor but are also affected by authigenic/hydrogenous processes and thus contribute to the apatite/authigenic factor in the 22-element QFA.

The remaining 4% of the variance that is not explained by these four factors can be explained by other minor sources, variations in end-member compositions (e.g., different aluminosilicate source compositions), and authigenic processes changing the primary source composition. Increasing the number of factors (e.g., to five or six) in the 22-element QFA resulted in statistically insignificant factors (that is, explaining less than 2% of the variability, and thus below our "statistical detection limit" [*Pisias et al.*, 2013] and excluded from the final model). However, the extra factors may still provide clues to minor sediment components. Two additional factors, not shown here, each explain about 1% of the variability with one having high-factor scores for Mg and the other for K. These could represent Mg-enriched and K-enriched altered ashes and/or authigenic minerals. Additionally, barite within the hydrothermal sediment can influence trace element concentrations and introduce variability into the data set, but given that elemental Ba in the data set is only greater than 1 wt % in 17 of 138 samples, we consider it overall to be a minor component of the sediment and accordingly exclude it from the model.

5.3. Bulk Pelagic Clay Characterization: CLS Multiple Linear Regression

Using the QFA results as guidance, we constructed a CLS multiple linear

Table 1. End-Member Compositions Used in the Constrained Least Square (CLS) Multiple Linear Regression Modeling of Bulk Pelagic Clay

Reference	End-Member	Si (wt %)	Al (wt %)	Ti (wt %)	Fe (wt %)	Mn (wt %)	Ca (wt %)	K (wt %)	P (wt %)
Taylor and McLennan [1985]	PAAS	29.35	10.00	0.60	4.55	0.09	0.93	3.07	0.07
Marchig and Erzinger [1986]	Idealized Hydrothermal	0	0.2	0.02	31.36	11.64	0	0	0
Barrett et al. [1987, Table 2b]	Metalliferous Sediment DSDP Leg 92	0	0.81	0.11	32.70	9.59	2.62	0.14	0
Takebe [2005]	CFA	0	0	0	0	0	40.48	0	16.27
Dymond and Eklund [1978, Table 2]	Fish Debris	0.03	0.11	0.01	0.22	0.21	32.29	0.05	15.00
Calculated	Pure Si	100	0	0	0	0	0	0	0

regression model of the bulk pelagic clay data set to quantify the proportions of each of the sediment end-member that mixed to create each sample. For the CLS model of the bulk pelagic clay, we chose to model eight major elements (Si, Al, Ti, Fe, Mn, Ca, K, and P) using four end-member compositions corresponding to the aluminosilicate, Fe-Mn oxyhydroxide, apatite, and excess Si factors identified by the QFA (Table 1).

We constructed multiple CLS models that separately used PAAS, Upper Continental Crust (UCC), rhyolite, dacite, and andesite compositions to successively represent the single general aluminosilicate factor, while the other three end-member compositions used in the model were held constant. These five CLS models calculated end-member proportions that exhibited similar patterns to each other when plotted downhole. The model with PAAS yielded the highest coefficients of determination and also explained the highest fraction (percentage) of the data set among the five options. We thus selected PAAS to represent the general aluminosilicate component in the bulk sediment.

Two apatite end-member compositions were also tested in the CLS model of bulk pelagic clay. The first was a fish debris composition determined by microprobe analysis [*Dymond and Eklund*, 1978]. The second was a pure apatite composition calculated from carbonate fluorapatite (CFA) stoichiometry [*Takebe*, 2005], with the other major elements set to zero as their abundance in apatite is negligible relative to Ca and P. There was $<$1% difference between the calculated end-member proportions for every sample in the two models. Both models also yielded high coefficients of determination indicating that both apatite compositions were effective end-members. We thus averaged the end-member proportions of each sample resulting from the two models.

Although the Fe/Mn ratio in the SPG marine sediment changes with distance from the MOR, we used a pure hydrothermal end-member to represent the third Fe-Mn oxyhydroxide QFA factor. Hydrothermal bulk sediment analyses in the literature do not commonly differentiate between pure hydrothermal deposition and the altered basalt or authigenic minerals enriched by hydrothermal inputs of Fe and Mn. For example, *Marchig and Erzinger* [1986] analyzed Deep Sea Drilling Program (DSDP) Leg 92 East Pacific Rise hydrothermal sediment on a carbonate-free basis and determined that even their most hydrothermally rich samples in fact were only 92% hydrothermal material. The remaining 8% was altered basalt. As we are trying to discriminate between the aluminosilicate and hydrothermal fractions of the bulk sediment, it would be inappropriate to consider such a mixture as a pure end-member. However, *Marchig and Erzinger* [1986] determined the composition of their 92%–8% mixture based on their own mixing model using tholeiitic basalt, continental crust, and a theoretical pure hydrothermal end-member. Therefore, we use the theoretical hydrothermal end-member of *Marchig and Erzinger* [1986] to represent our Factor 2.

To check that this theoretical hydrothermal end-member was reasonable and a good choice for an end-member, we ran the model separately with the average composition of the metalliferous component of Leg 92 sediment from *Barrett et al.* [1987], who were careful to differentiate the Fe-Mn oxyhydroxide portion of hydrothermal deposition from the aluminosilicate fraction. The difference between the end-member proportions of these two models on a sample-by-sample basis was between 0 and 10% and averaged ~ 1%. Both end-members produced results with high coefficients of determination. We therefore constructed four CLS models that used each Fe-Mn oxyhydroxide end-member with each of the apatite end-members and averaged the end-member proportions resulting from the four models. Each of the four models explained $>$ 89% (on average, 99%) of the compositional data of each sample.

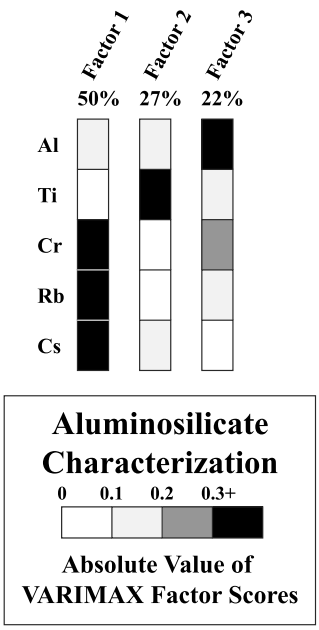

Figure 4. Factors 1, 2, and 3 produced by the aluminosilicate element $QFA_{aluminosilicate}$ modeling. Diagram is structured similar to Figure 3 with the same scale bar.

We used pure Si to represent the excess Si factor. To explore variations in this end-member, we also ran the model with a diatom frustrule composition [*Loucaides et al.*, 2010] that included trace amounts of Al and K. However, the pure Si produced higher coefficients of determination for each element and explained a higher fraction of the data set, possibly because diatom frustrules may not be representative of the altered radiolarian composition from the center of the SPG due to species differences or the low dust flux in the SPG changing the Al concentration of open ocean biogenic siliceous material.

6. Specific Discrimination of Aluminosilicate Sources

In this section, we focus exclusively on the aluminosilicate fraction of the sediment, which to this point we have carefully only referred to as a "general aluminosilicate component," which has been sufficient for (and required by) the broad characterization of the pelagic clay. However, partitioning of this general aluminosilicate component into PAAS, rhyolite, and mafic components is warranted, and we are able to differentiate provenance variations with a higher fidelity. We refer to these specific QFA and CLS treatments targeting the aluminosilicate component(s) as "$QFA_{aluminosilicate}$" and "$CLS_{aluminosilicate}$" so as to differentiate them clearly from the general characterization statistical work described above.

6.1. Aluminosilicates: Q-Mode Factor Analysis ($QFA_{aluminosilicate}$)

To determine the composition of the aluminosilicate fraction of the sediment, and only the aluminosilicate fraction, we selected elements most strongly associated with the Factor 1 "aluminosilicate" end-member from the broad 22-element QFA (Ti, Al, Cr, Rb, and Cs) for the $QFA_{aluminosilicate}$. We excluded K and Mg because their concentrations can be affected during ash alteration and/or the formation of other authigenic minerals, and the goal of this study is to model the primary (original) source end-member composition(s). Rb and Cs can also be affected by ash alteration [*Yamamoto et al.*, 1986] but are commonly associated with the detrital fraction of pelagic sediment [*Li and Schoonmaker*, 2003]. At Sites U1365, U1366, U1369, and U1370, a simple linear regression fit to concentrations of Cr versus Rb has a r^2 of 0.8 and Cr versus Cs has a r^2 of 0.9, suggesting strong relationships among these elements. Their relationship is also reflected in the results of every $QFA_{aluminosilicate}$ iteration we performed, which consistently indicated that Rb and Cs covary strongly with Cr. Considering that Cr has very different chemical behavior than Rb and Cs, this suggests that the elements are a good selection to identify primary provenance; consequently, we retained these elements in our models.

The $QFA_{aluminosilicate}$ statistical runs with this aluminosilicate element menu produced three factors that explained 98% of the data set variability (Figure 4 and Table S4). The first factor explains 50% of the variability of the data set and indicates that Cr, Rb, and Cs covary strongly. We interpret this factor as an intermediate composition, continental aluminosilicate because the QFA factor loadings indicate that this factor is more important in samples that plot near PAAS and UCC values in the Ti/Al profiles and several ternary diagrams (Figures 2f and 5). We interpret the second factor, which isolates Ti and explains 27% of the variability, as representing a high Ti/Al, mafic, aluminosilicate source because the factor loadings indicate that this factor is most important near the basement of each site and in intervals with higher Ti/Al (Figure 2f). The third factor explains 22% of the variability and has strong factor scores for Al. The

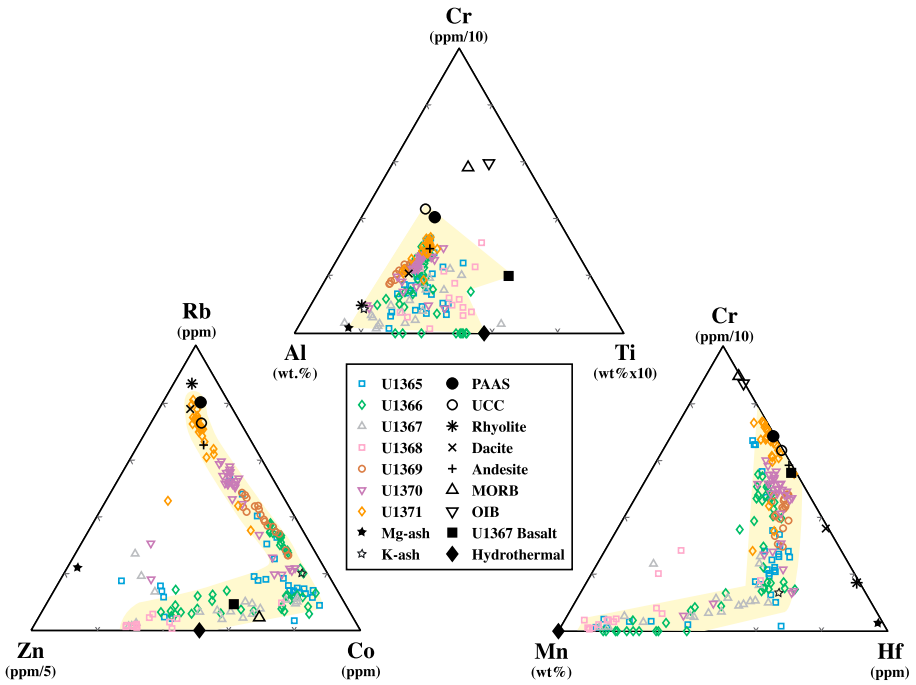

Figure 5. Samples from the seven sites drilled during Expedition 329 plotted on ternary diagrams with end-member compositions including samples that primarily consist of calcareous and siliceous material. To construct the ternary diagram, element concentrations were scaled (as noted in the units of each plot) to be of comparable magnitude with the other elements in the plot and then normalized so the three element concentrations sum to a constant. This later step is common to all ternary diagrams and allows each ternary plot to graphically depict the ratio of the three elements as positions in an equilateral triangle. Highlighted in yellow are intersite patterns that express clusters determined by paleogeographic position. For example, sites geographically closer to and downwind of Australia (e.g., Site U1370 and Site U1371) plot closer to continental sources such as post-Archean average Australian shale (PAAS). End-members plotted are listed in Tables 1 and 2.

factor loadings show that this third aluminosilicate factor is important in samples with a lower Ti/Al ratio, which we interpret as representing a felsic, rhyolite composition, as suggested by the Ti-Al-Cr ternary diagram (Figure 5) and the discrete ash layers from the SPG. The three aluminosilicate factors are consistent with and therefore reinforce the interpretations of the ratio plots and ternary diagrams that together suggest three distinct aluminosilicate sources. When we forced a QFA analysis to increase the number of factors, a fourth factor explained the remaining 2% of the data set variability. We consider the fourth factor to be statistically insignificant and conclude that the variability of the data set can best be explained by the mixing of the first three factors.

6.2. Aluminosilicates: $CLS_{aluminosilicate}$ Multiple Linear Regression

Because the $QFA_{aluminosilicate}$ suggested three end-members, we ran iterations of the CLS model using every combination of three end-members from a list of 20 possible aluminosilicate end-members to objectively test which combination(s) yield(s) the CLS model that best fits the data set. These 20 possible end-members (Table 2) include upper crustal sources (e.g., PAAS, Chinese Loess, UCC, and dacite), mafic sources (e.g., average mid-ocean ridge basalt (MORB), oceanic island basalt (OIB), andesite, and basalts drilled during Expedition 329), and felsic sources (e.g., average rhyolite and discrete SPG ash layers). We recorded the goodness-of-fit parameters for each CLS model iteration and identified the models that yielded the highest coefficients of determination. The 10 CLS models that best fit the data set included one end-member from each of the three categories of aluminosilicate end-members indicated by the Ti/Al ratio, ternary diagrams, and the $QFA_{aluminosilicate}$, that is, a continental aluminosilicate, a rhyolite, and a mafic source. We discuss these end-member results in sequence below.

6.2.1. Continental Aluminosilicate End-Member

PAAS and Chinese Loess produced similar model outcomes, due to their similar chemistries, with the highest coefficients of determination (0.92–1.00) and explained ~99.9% of the data set. Other dust compositions,

Table 2. End-Member Compositions Tested in the Constrained Least Square (CLS) Multiple Linear Regression Model of the Aluminosilicate Component of the Pelagic Clay[a]

Reference	End-Member	Al (wt %)	Ti (wt %)	Cr (ppm)	Rb (ppm)	Cs (ppm)
Taylor and McLennan [1985]	Post-Archean Australian Average Shale (PAAS)	10.00	0.60	110.00	160.00	15.00
Taylor and McLennan [1985]	Upper Continental Crust (UCC)	8.04	0.30	35.00	112.00	3.70
Rudnick and Gao [2003, Table 11]	Upper Continental Crust (UCC)	8.13	0.38	92.33	82.00	4.10
Taylor et al. [1983]	Chinese Loess	8.15	0.47	69.00	108.00	7.70
Compiled by *Plank and Langmuir* [1998]	GLOSS	6.30	0.37	78.90	57.20	3.48
Gromet et al. [1984]	NASC	8.94	0.42	124.50	125.00	5.16
This study (Table S2)	Mg-ash 329-U1366F-3H4-100/101 (19.5 mbsf)	7.48	0.14	1.82	17.17	0.34
This study (Table S2)	K-ash 329-U1370D-7H6-70/72 (61.7 mbsf)	7.30	0.16	8.90	71.58	1.11
GeoRoc database	Rhyolite Average	7.23	0.15	9.50	131.63	5.54
GeoRoc database	Dacite Average	8.38	0.37	32.05	98.57	6.74
GeoRoc database	Andesite Average	8.89	0.53	59.97	68.85	4.18
GeoRoc database	Basalt Average	8.96	0.75	152.17	29.98	1.50
Gale et al. [2013, Table 2]	ALL MORB Mean	7.78	1.01	249.00	2.88	0.03
Willbold and Stracke [2006]	Average South Pacific OIB	7.02	1.85	378.29	30.06	0.37
Zhang and Smith-Duque [2014]	Altered Basalt U1368 Average	7.48	1.29	213.04	8.89	0.51
Zhang and Smith-Duque [2014]	Altered Basalt U1365 Average	8.59	0.72	276.15	15.33	0.41
Dzaugis et al. [2013]	Site U1365 basalt avg ($n = 14$)	7.94	0.93	223.40	6.25	0.12
Dzaugis et al. [2013]	Site U1367 basalt avg ($n = 5$)	7.20	1.59	58.23	7.15	0.42
Dzaugis et al. [2013]	Site U1368 basalt avg ($n = 21$)	7.56	1.31	248.46	8.04	0.31
Dzaugis et al. [2013]	Sites U1365, U1367, U1368 basalt avg ($n = 40$)	7.65	1.21	215.91	7.30	0.26

[a]The references for each end-member composition are listed in the first column. Rhyolite, dacite, andesite, and basalt are average compositions of whole rocks from New Zealand, Central and South America downloaded from GEOROC database accessed March 2014 (http://georoc.mpch-mainz.gwdg.de/georoc/). Prior to averaging the GEOROC data, elements were plotted against Al and extreme outliers were removed. The Mg ash and K ash are discrete altered ash layers from Sites U1366 and U1370, respectively, that were analyzed in this study (see Table S2). The low-Cr basalt was an average of five basalt samples drilled at Site U1367 and analyzed on the ICP-ES and ICP-MS at Boston University [*Dzaugis et al.*, 2013].

such as UCC, produced CLS models with acceptable, but lower, coefficients of determination (0.71–1.00). We selected PAAS to represent the intermediate end-member because (i) significant quantities of Chinese Loess are unlikely to be transported to the SPG given global wind patterns [*Li et al.*, 2008], and (ii) Australian dust is directly upwind of the sites, making it a geologically reasonable end-member [*Mackie et al.*, 2008].

6.2.2. Rhyolite End-Member

The $CLS_{aluminosilicate}$ models with the highest goodness-of-fit parameters consistently use a generic whole-rock rhyolite (Table 2) or one of two discrete ash layers with rhyolitic compositions (from Sites U1366 and U1370) to represent the low Ti/Al end-member. Although the discrete ash layers are bulk analyses and possibly include hydrogenous and/or Fe-Mn oxyhydroxide components in their composition, the proportions of the specific elements being used to model the aluminosilicate fraction should remain relatively unaffected [*Li and Schoonmaker*, 2003]. Indeed, the ash layers may represent a more accurate end-member composition than the whole-rock analyses because they are a known part of the sedimentary material. Because the three compositions each produced excellent and comparable models (average coefficient of determinations between 0.92 and 0.96) and there is no *a priori* reason to favor one over the other, we averaged the results of the $CLS_{aluminosilicate}$ models run separately with these three ash compositions. Standard deviations of the end-member contributions determined by the three models averaged 11%, 9%, and 3% for the PAAS, rhyolite, and mafic end-members, respectively. These values help give a sense of the true precision of the statistical approach (that is, ~ 5–10% of the quantified abundances of the end-members).

6.2.3. Mafic Aluminosilicate End-Member

The high Ti/Al end-member is surprisingly difficult to model and presents some subtle challenges. As observed in the Al-Ti-Cr ternary diagram (Figure 5) and supported by the results of the $CLS_{aluminosilicate}$ models, average OIB and MORB compositions [e.g., *Willbold and Stracke*, 2006; *Gale et al.*, 2013] have Cr

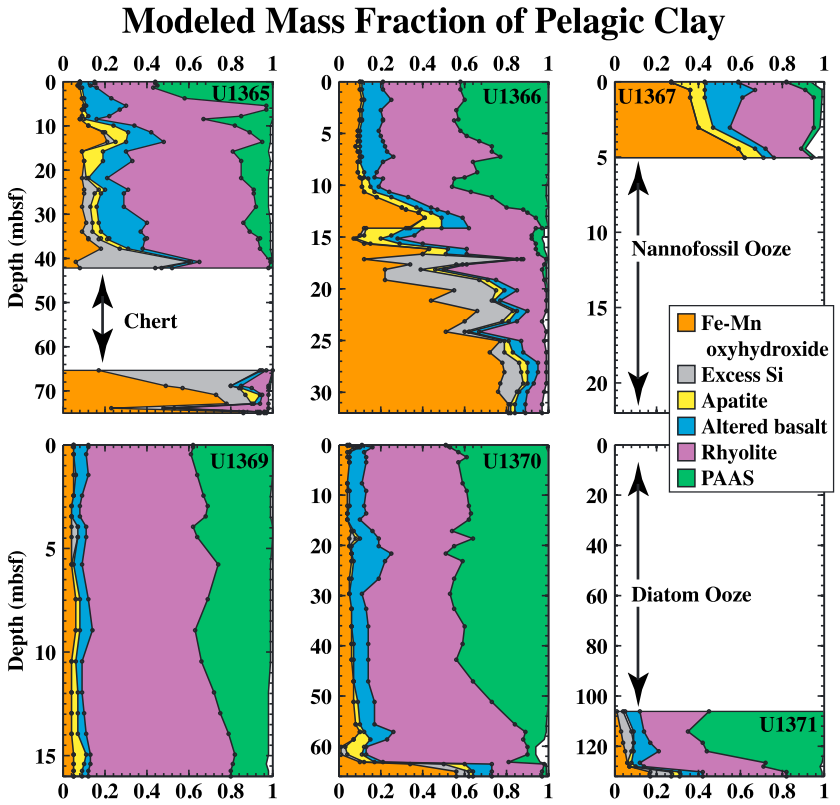

Figure 6. The relative mass fractions of six end-members produced by the bulk pelagic clay and $CLS_{aluminosilicate}$ multivariate models. At Site U1365, the interval from 42 to 65 mbsf is chert that was not analyzed in this study. At Site U1367, calcareous sediment is the dominant lithology from 5 mbsf to the basalt (22 mbsf). At Site U1371, siliceous deposits dominate the lithology from the seafloor to 104 mbsf and are not included in the CLS models (see text).

concentrations that are too high to encompass the sample compositions. Instead, a high Ti/Al, relatively low-Cr end-member is needed. The Al-Ti-Cr ternary diagram suggests an end-member similar to the Site U1367 basalt composition, although a hydrothermal source would also satisfy these initial constraints. The Site U1367 basalt is an average of five unaltered basalt samples from Site U1367 analyzed at Boston University [*Dzaugis et al*., 2013], and its Cr concentration (58 ppm) is within the wide range commonly found in basalts drilled during Expedition 329 (~30–730 ppm) [*Zhang and Smith-Duque*, 2014] and in OIBs (3–1290 ppm) [*Willbold and Stracke*, 2006].

The Ti/Al of the U1367 basalt (0.22 g/g) is also higher than an average MORB composition (0.13 g/g) [*Gale et al*., 2013] but is lower than an average OIB composition (~0.26 g/g) [*Willbold and Stracke*, 2006]. Eroded basaltic grains are observed in the sediment [*D'Hondt et al*., 2011], and it is likely that still more of this eroded source has since been altered to authigenic clay [e.g., *Kastner*, 1999]. Such authigenic clay is likely to retain at least its approximate Ti and Al signature. However, this basaltic source (either now altered or not) is also going to be broadly stratigraphically coincident with enriched Fe-Mn-oxyhydroxides from hydrothermal sources, and this hydrothermal source may also include at least some Al and Ti sourced from seawater and incorporated into or onto the hydrothermal particulates. However, given that the basalt component describes only a relatively small part of the bulk sediment (averaging 8% and always less than 24%), and the hydrogenous fraction is even smaller, this approach has minimal impact to our broad-scale interpretations of the paleoceanographic evolution of the SPG. Therefore, we selected the U1367 basalt to collectively represent a high Ti/Al, altered basalt source.

7. End-Member Mass Accumulation Rate Patterns Through the Cenozoic

The $CLS_{aluminosilicate}$ analysis yields the fractions of the aluminosilicate component that are PAAS, rhyolite, and altered basalt in each sample. To estimate the fraction of PAAS, rhyolite, and altered basalt in the total

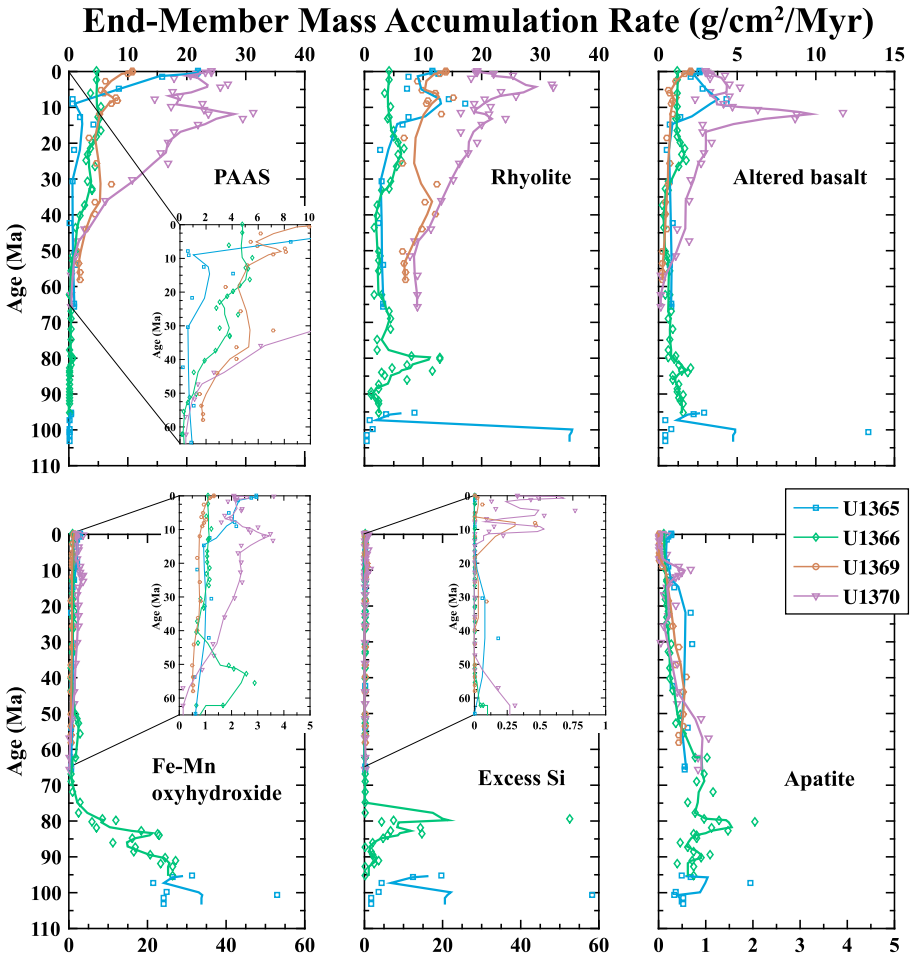

Figure 7. The mass accumulation rate (g/cm^2/Myr) of each end-member at the four sites dominated by pelagic clay lithology, Sites U1365, U1366, U1369, and U1370. The symbols (denoted in the legend) mark the MAR of each sample and the lines depict a 3-point moving average of the samples. Inset graphs emphasize smaller-scale mass accumulation rate variations from 65 to 0 Ma.

bulk sediment, we weighted the $CLS_{aluminosilicate}$ results with the mass fraction of total aluminosilicate in bulk sediment determined by the general sediment characterization CLS model (Figure 6 and Table S5). For example, if the general characterization CLS determines that 50% of a bulk sample is aluminosilicate, and the $CLS_{aluminosilicate}$ reveals that 50%, 30%, and 20% of that aluminosilicate portion is PAAS, rhyolite, and altered basalt, respectively, the total bulk sediment includes 25% PAAS, 15% rhyolite, and 10% altered basalt.

For subsequent paleoceanographic interpretations, we calculated ages and instantaneous sedimentation rates from a Co-based technique for each pelagic clay sample from Sites U1365, U1366, U1369, and U1370 [*Dunlea et al.*, 2015]. By multiplying the instantaneous sedimentation rate (in cm/Myr) with the dry bulk density (in g/cm^3) of each sample, we acquire the bulk sediment mass accumulation rate (MAR, in g/cm^2/Myr). The product of the bulk sediment MAR and the mass fractions of each end-member determined by the CLS models yields the MAR of each end-member (in g/cm^2/Myr) (Figure 7 and Table S5). In the following sections, we interpret the end-member MAR patterns at Sites U1365, U1366, U1369, and U1370 along with the ternary diagrams using samples from all seven sites to highlight some of the key features of the paleoceanographic evolution of the SPG.

7.1. Fe-Mn Oxyhydroxides MAR Decreases With Distance From MOR

As documented in previous studies of Fe-Mn-enriched hydrothermal deposition, the MAR of the Fe-Mn oxyhydroxide component decreases rapidly at Sites U1365 and U1366 as they migrate away from the MOR

[e.g., *Lyle*, 1986; *Marchig and Erzinger*, 1986]. Our results show that this classic pattern provides further confidence in our modeling approach. Our age model for Site U1370 does not extend below the carbonate layer, which prevents calculation of MARs at this depth. Three samples, however, located below this layer show higher-mass fraction of Fe-Mn oxyhydroxides in a thin, 2 m interval directly above the basement (Figure 6). Although Site U1369 was drilled to basement, the interval of hydrothermal deposition was thin [*D'Hondt et al*., 2011] and was not sampled. The modeled mass fractions at Site U1367 (Figure 6) show a high contribution of Fe-Mn oxyhydroxides relative to the other components, which is likely due to its current proximity to the MOR and distance from a continental dust or volcanic ash source [*D'Hondt et al*., 2011].

7.1.1. Hydrothermal Deposition From the Osbourn Trough?

Intervals of hydrothermal-rich deposition overlying the basement are thicker at Sites U1365 and U1366 than at Sites U1369 and U1370. This may reflect that Sites U1365 and U1366 recorded local variability in hydrothermal input due to bathymetry (e.g., ponding or lack thereof), deep ocean currents, or some other local process.

Alternatively, Sites U1365 and U1366 may have experienced higher hydrothermal input due to tectonic processes relating to their locations in the Late Cretaceous. For example, Sites U1365 and U1366 are located directly next to the Osbourn Trough, a failed ridge system that ceased spreading in the Late Cretaceous between ~71–84 Ma [*Billen and Stock*, 2000] and 87–97 Ma [*Downey et al*., 2007]. Using the approximated basement age estimate of ~95 Ma for Site U1366 [*Dunlea et al*., 2015], rapidly accumulating hydrothermal deposition begins decreasing at ~85 Ma and reached generally present-day levels by 70 Ma (Figure 7). With the range of possible basement ages for Site U1366 (85–105 Ma, [*Dunlea et al*., 2015]), the decline may have begun any time between ~75 Ma and 90 Ma, which is when the Osbourn Trough is thought to have gone extinct. The geochemical record at Site U1366 has a subtle pulse of hydrothermal activity at ~55 Ma (Figure 7), which may indicate a brief and final reemergence of hydrothermal activity from the Osbourn Trough. A closely related potential explanation of the decreasing hydrothermal deposition at Sites U1365 and U1366 relates to the backtracked paths, which suggest that Sites U1365 and U1366 may have migrated parallel to the Osbourn Trough until ~80 Ma, when they began to migrate north away from the MOR (Figure 1). The decrease in hydrothermal input may reflect this change in plate motion.

7.2. Temporal and Spatial Changes in Biogenic Siliceous Accumulation

The Late Cretaceous (~100–75 Ma) was a period of high excess Si MAR at Sites U1365 and U1366 caused by increased biogenic siliceous deposition that has been preserved as frustules or in Si-enriched authigenic mineral phases (Figure 7). This period of high excess Si is not seen at Site U1369, despite a backtrack path that suggests similar paleolocations (Figure 1).

A more subtle increase in the accumulation of excess Si at Sites U1369 and U1370 occurred at ~10–8 Ma. This increase at these two sites coincided precisely with the transition from pelagic clay to siliceous ooze at Site U1371 that has been dated paleomagnetostratigraphically and biostratigraphically at ~8.5 Ma [*Cortese and Alvarez Zarikian*, 2015; *Suto and Uramoto*, 2015]. Site U1371 is currently located on the outer edge of the SPG to the southwest of Sites U1369 and U1370.

Changes in biogenic Si MAR reflect either a change in export production, preservation, or both. There is no independent reason why the preservation of biogenic Si would change dramatically on this geographic scale, given seawater's global and continual undersaturation with respect to silica [e.g., *Ragueneau et al*., 2000]. Therefore, we interpret the increase in biogenic Si MAR to reflect an increase in export production, caused by changes in water masses, nutrient supply, or other aspects of the biogeochemical cycle of Si. We note the transition to more siliceous sediment in the southern sites coincided with the so-named "Carbonate Crash" from 11 to 8 Ma in the eastern and central Pacific and closure of the Isthmus of Panama, consistent with a significant reorganization of ocean currents, nutrient distributions, and/or phytoplankton production at this time [e.g., *Lyle et al*., 1995; *Pälike et al*., 2012; *Alvarez Zarikian*, 2015].

While tectonic processes may have shifted nutrient regimes by reorganizing ocean currents, changes in eolian dust and ash deposition could also have been a source of nutrients capable of stimulating productivity in the distal open ocean. For example, Sites U1369, U1370, and U1371 are currently located between the center of the SPG, which is primarily N limited, and the Southern Ocean, which is primarily Fe limited [*Moore et al*., 2013]. Considering the potential geographic and temporal variability of these nutrient

regimes from changing water masses in concert with the northward migration of Sites U1369, U1370, and U1371 over time, it is possible that the inferred changes in export production at these sites reflect differences between a N- and Fe-limited regime. For example, the higher MAR of dust and ash at ~10–8 Ma as observed at some of the SPG sites (Figure 7) could provide the surface ocean with limiting nutrients causing increased export production and the increase in excess Si observed at Sites U1369, U1370, and U1371.

7.3. Australian Dust: Spatial and Temporal Patterns

7.3.1. Spatial Extent of Australian Dust Deposition

Currently, Australian deserts are the largest dust source by mass in the Southern Hemisphere [*Mackie et al*., 2008]. With the prevailing westerlies located between ~30 and 60°S, Australia is the dominant source of dust in the South Pacific and much of the Southern Ocean [*Li et al*., 2008]. Relative to Australia, Antarctica is an insignificant source of dust to the Southern Hemisphere and the SPG [*Li et al*., 2008]. If it contributed more dust to the SPG in the past, perhaps during the initial aridification of Antarctica, it would be combined with the PAAS component in our model and is most likely to influence the more southern sites (Sites U1371 and U1370) when they were south of ~60°S early in the Cenozoic (Figure 1). However, our results support Australia as the predominant source of dust to the SPG.

Compositional trends in the sediment from the seven sites analyzed in this study correlate with the spatial relationship between each site and Australia. Sites U1371 and U1370, the sites closest to and most directly downwind of Australia (Figure 1), are compositionally closer to PAAS than the other sites (Figure 5). Additionally, sites distal from Australia show stronger authigenic enrichment from processes that concentrate elements in sediment with long seawater exposure times, such as scavenging on oxides and/or incorporation into fish debris. For example, samples from Site U1369, which is downwind but farther away from Australia than Sites U1371 and U1370, plot on a smooth compositional array that demonstrates mixing between PAAS and an authigenically enriched component represented by Co and Hf (Figure 5). Samples from Sites U1365 and U1366 plot on an array between hydrothermal-enriched elements (Mn and Zn) and authigenic-enriched elements (Co and Hf), as well as along a second array from the authigenic-enriched component toward PAAS (Figure 5). These arrays are remarkably consistent in a number of different diagrams.

All of the pelagic sediment samples, including clay, siliceous, and calcareous lithologies, plot within this trend, from a mainly hydrothermal enriched composition to a more authigenic-enriched composition and then to a PAAS end-member. The Al-Ti-Cr and Mn-Hf-Cr ternary diagrams suggest the presence of ash components but still exhibit trends toward PAAS. This result reinforces that sites downwind and closer to Australia trend toward PAAS and not an ash composition. The Australian input is clear and spatially consistent.

7.3.2. Australian Dust Deposition Through the Cenozoic

At the beginning of the Cenozoic, Australia was covered in rainforests supported by a climate that was much warmer and more humid than today [*Martin*, 2006]. The terrestrial vegetation record indicates that progressive cooling and aridification of Australia occurred in multiple steps that coincided with global climate trends. While the aridification occurred gradually throughout the Cenozoic, the first major transition from warm-humid climates to cool-dry climates in Australia occurred in the mid-Miocene [*Martin*, 2006]. The cooling trend continued through the Miocene to present, interrupted by a brief period of wetter climate in the early Pliocene.

Our marine records track how the cooling and drying of Australia affected the deposition of dust in the open ocean SPG through the Cenozoic (Figures 7 and 8). Just after the Early Eocene Climatic Optimum (at ~50 Ma) [*Zachos et al*., 2001], the MAR of PAAS began increasing at Sites U1366, U1369, and U1370. While all of these sites were downwind from Australia at this time (Figure 1), the MAR of PAAS increased more rapidly at Site U1370 than at Sites U1366 and U1369, most likely because Site U1370 was closer to the Australian continent. Plate reconstructions suggest that Site U1365 was located north of Australia, which would not have been in the wind path from the continent, and thus would not have experienced a coeval increase in dust MAR at the same time as the more southern sites. The synchronous increase at multiple sites precludes the possibility that this PAAS increase occurred exclusively because a site tectonically migrated closer to Australia, the source of dust.

After the early Eocene, there was an overall increase of the MAR of PAAS at each site. However, the increase was not a smooth gradual trend but was punctuated by abrupt increases and decreases from the Miocene to present. Even with the slow sedimentation rates at these sites, we can begin to correlate some common trends in the MAR of PAAS in the SPG sites and relate it to dust accumulation records from other studies in the South Pacific. Collectively, these records suggest at least three traceable episodes of increased dust accumulation in the SPG from the Miocene to the present.

Below, we discuss the evidence for multiple episodes of increased dust accumulation across the SPG and suggest the timing of each episode based on our current preferred age model. The exact timing of these three episodes and subsequent interpretations may be adjusted in the future with updated age models. Furthermore, slight differences in our own age model determinations can impart variations in the PAAS MAR (e.g., see Figure S1 for the PAAS MAR record using variations in the age model described in *Dunlea et al*. [2015]).

The first and most obvious local maximum of dust MAR occurred around the mid-Miocene (15–10 Ma), when the terrestrial vegetation record suggests that Australia experienced its first major shift from a warm-humid to cool-dry climate [*Martin*, 2006]. Relatively close to the eastern coast of Australia (<1000 km) at DSDP Sites 588, 590, and 591, dust accumulation doubled during the mid-Miocene from ~200 to ~500 g/cm^2/Myr, as estimated by the smectite/illite ratio [*Stein and Robert*, 1986]. At Site 596, dust accumulation, determined using statistical partitioning techniques, abruptly increased from 0 to ~15 g/cm^2/Myr between 13 and 10 Ma [*Zhou and Kyte*, 1992]. Despite lower resolution sampling, this increase is also seen at Site U1365, located ~350 km west of Site 596 and is also subtly, yet clearly, present farther from Australia at Site U1366 (Figure 7). Site U1370 shows a very obvious maximum in PAAS accumulation, increasing from ~20 g/cm^2/Myr up to ~30 g/cm^2/Myr, between 13 and 10 Ma (Figure 7). Geographically close to Site U1370, core MV0502-01JC (40°00'S, 154°02'W; Figure 1) had rapid accumulation of eolian material at ~10 Ma, as determined by fish teeth stratigraphy, operationally defined leaching techniques, and mineralogy [*Stancin et al*., 2008]. After this pulse of dust MAR between ~15 and 10 Ma, all of these sediment records show that dust MARs returned to previous levels shortly after 10 Ma.

There was a second pulse of dust at ~6 Ma at some of the sites, including Site 588 and core MV0502-01JC [*Stein and Robert*, 1986; *Stancin et al*., 2008]. At Sites 596 and U1365, the detrital accumulation rate also abruptly increased at ~6 Ma. The small increase in PAAS MAR at Site U1369 at ~8 Ma may be evidence of the first episode of dust, given the tolerance of the age model, or could be a combined signal from the first and second episodes. Although subtle features at U1370 may represent this dust pulse, the sampling resolution is too low for this time period to adequately resolve it.

A third pulse of dust at ~4–3 Ma occurred at DSDP Sites 588, 590, 591, our IODP Site U1370, and core MV0502-01JC [*Stein and Robert*, 1986; *Stancin et al*., 2008]. At Sites 596 and U1365, however, this third pulse is indistinguishable from the second pulse that started at ~6 Ma, but at Site 596 there was a distinct increase in detrital MAR from ~15 g/cm^2/Myr to ~30 g/cm^2/Myr at ~3 Ma. The terrestrial record [*Martin*, 2006] indicates that just before this third pulse, in the early Pliocene (~5 Ma), there was a brief period of warm-humid climate that interrupted the overall cooling and aridification of Australia throughout the Cenozoic. There was a resurgence of rainforest in parts of southeast Australia, suggesting increased rainfall [*Martin*, 2006], which would stimulate vegetation cover and reduce dust activity [*Mackie et al*., 2008]. These processes along with fluvial transport may have increased the transport and erodibility of soils in the region. After the early Pliocene warm period ended and the climate returned to being cool and dry in the late Pliocene, there likely was an increased amount of dust to be blown to the sea creating the pulse of dust at ~4–3 Ma.

In summary, three major episodes of rapid Australian dust MAR between the mid-Miocene and the present occurred at multiple sites located at varying distances from Australia. These episodes are superimposed on an overall increase in dust MAR at the SPG sites since the early Eocene.

7.3.3. Regional and Global Aridification Linked to Opening of Ocean Gateways

The initial increase in PAAS at Sites U1366, U1369, and U1370 at ~ 50 Ma coincides with the earliest evidence of the Tasman Gateway opening just after the Early Eocene Climatic Optimum [*Bijl et al*., 2013]. However, the majority of the Tasman Gateway deepened between 36 and 30 Ma when Sites U1366 and U1369 experienced a local maximum of PAAS MAR (Figure 7), suggesting the Tasman opening may have been a significant step in the aridification of Australia.

Did Australia aridify because the Tasman Gateway opened and Australia migrated into an arid air belt ~30°S? Or was the aridity a response to global cooling and aridification trends? The first hypothesis is supported by the terrestrial record, which suggests there was a steep climate gradient within the North West Shelf of Australia during the Eocene. The northern region experienced warm-arid climates while the region ~1800 km to the south experienced cooler and wetter climates. Further south, there was also considerable rainfall and runoff in Southern Australia [*Martin*, 2006]. The meridional climate gradient may indicate that the continent moved into downwelling air masses from Hadley Cell circulation and aridified northern Australia, while keeping the south moist with rainfall from upwelling air masses. The northward migration of Australia and changes in moisture transport may have affected Antarctic climate as well. Reconstructions of East Antarctica temperature and precipitation indicate that East Antarctica gradually aridified from ~54 to 13 Ma, with an abrupt increase in aridification at ~34 Ma [*Passchier et al.*, 2013], the same time as an episode of increased PAAS MAR at Sites U1366 and U1369.

Both Australia and Antarctica may have aridified in response to global cooling in the early Eocene and Eocene-Oligocene [*Zachos et al.*, 2001]. Although Sites U1366 and U1369 were located at different latitudes at ~34 Ma, the relative increase in PAAS MAR was of similar magnitude at both sites, suggesting that either there was not a significant meridional difference in Australian aridity or the westerlies transported dust from northern Australia farther southeast across the SPG. Thus, the SPG data cannot strictly exclude that the increase in Australian dust flux may have been a simple response to planetary global cooling. Although the preponderance of evidence, as well as "Occam's Razor," supports the meridional migration explanation, future studies should further examine whether both the migration and cooling were together responsible for the observed increase in Australian fluxes.

7.4. Explosive South Pacific Volcanism

The SPG is surrounded by explosive ash-emitting subduction-zone volcanism that encircles the Pacific Plate and includes the Andes to the east and New Zealand to the west. A few studies have examined the frequency of (altered) ash layers at multiple sites in the South Pacific to estimate volcanic activity throughout the Cenozoic, including just off the eastern coast of Australia [*Gardner et al.*, 1986], east of New Zealand [*Carter et al.*, 2004], the Andes [*Noble et al.*, 1974], and the entire Pacific Ocean [*Straub and Schmincke*, 1998]. Episodes of increased volcanism can be broadly summarized as having occurred around one or more of these intervals: 110–70 Ma, ~40–35 Ma, 26–24 Ma, 15–10 Ma, ~4 Ma, and 2–0 Ma. While these intervals of increased frequency of ash layers do not occur at every site, possibly due to poor preservation due to water depth and local oceanographic conditions, the mid-Miocene (~15–10 Ma) episode is the most common and clear feature among the sites.

In our study, we quantify dispersed ash (rhyolitic and basaltic) in the bulk sediment rather than the discrete ash layer frequency. This focus on dispersed ash yields additional information about the volcanic record, in addition to studies based just on discrete ash layers [e.g., *Scudder et al.*, 2014]. The range in the MAR of rhyolite is comparable to the range of the MAR of PAAS. That these rates are relatively close in magnitude is consistent with modern observations of distal volcanic input to the deep sea [*Olgun et al.*, 2011]. The high abundance of dispersed ash is consistent with the very distal nature of the SPG and the large amount of explosive volcanism in the surrounding region. Along with quantifying the MAR magnitude, dispersed ash also allows us to avoid potential problems associated with ash layer preservation and/or loss of ash layers due to drilling.

Although sampling resolution at the SPG sites may be too low to resolve some of the short-lived episodes observed at other sites (cited above), the Cretaceous interval (110–70 Ma) of increased volcanism is apparent in the accumulation rate profiles of rhyolite at Sites U1365 and U1366. The mid-Miocene interval is also a notable feature at Site U1370 at ~13 Ma and at Site U1365 at ~10 Ma. These episodes of volcanism are superimposed on a longer-term trend of increasing ash deposition that roughly doubles throughout the Cenozoic. This Cenozoic trend of increasing deposition is seen at all the SPG sites. Collectively, the consistency between the records of ash accumulation in this study and the previously published records of volcanism from ash layer frequency indicates that the SPG faithfully records long-term records of volcanism.

7.4.1. Interrelationships of Aridity, Volcanic Activity, and Wind

Comparison of the collective dust and ash records reveals that many of the episodes of increased dust and ash MAR were broadly synchronous (Figure 7). For a more detailed look at this relationship, we

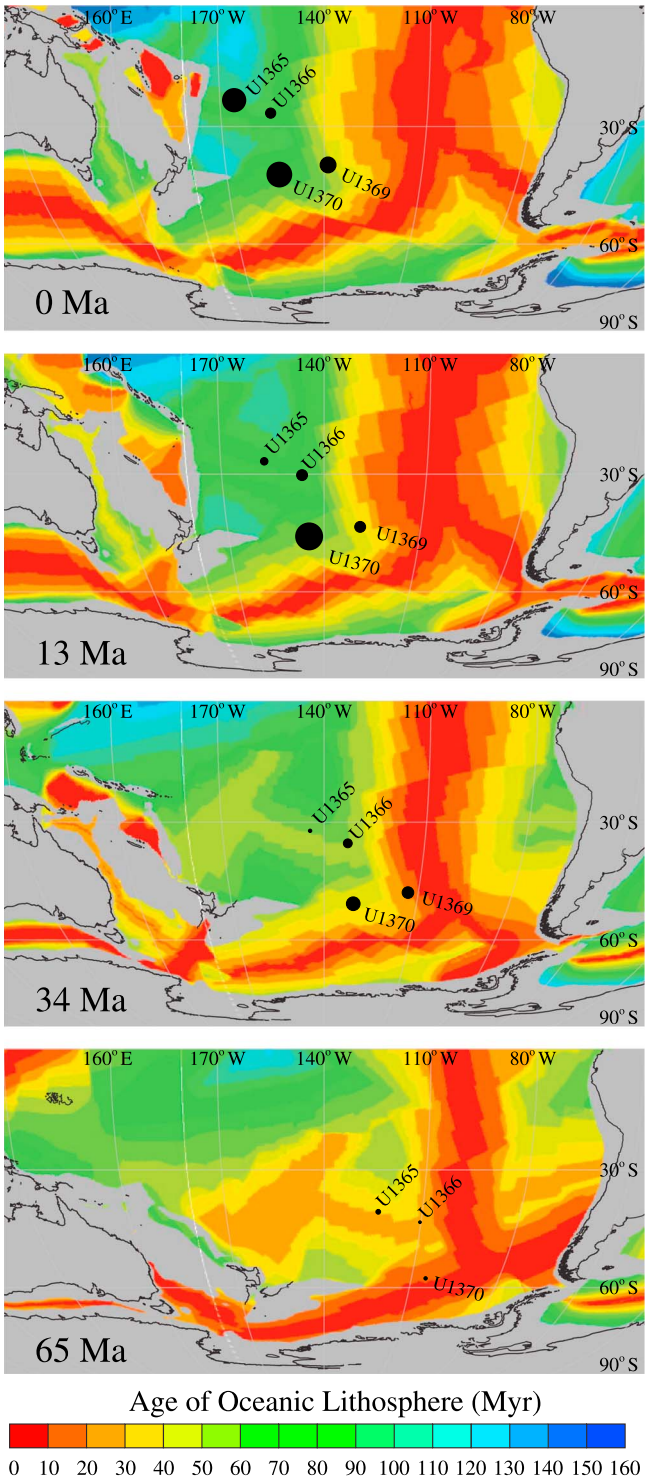

Figure 8. Mass accumulation rate of PAAS at various times through the Cenozoic. The center of each dot marks the location of a site backtracked to the time labeled on each map. The size of each dot is proportional to the MAR of PAAS (from Figure 7) at that site at the given time. Background maps are the same as described in Figure 1.

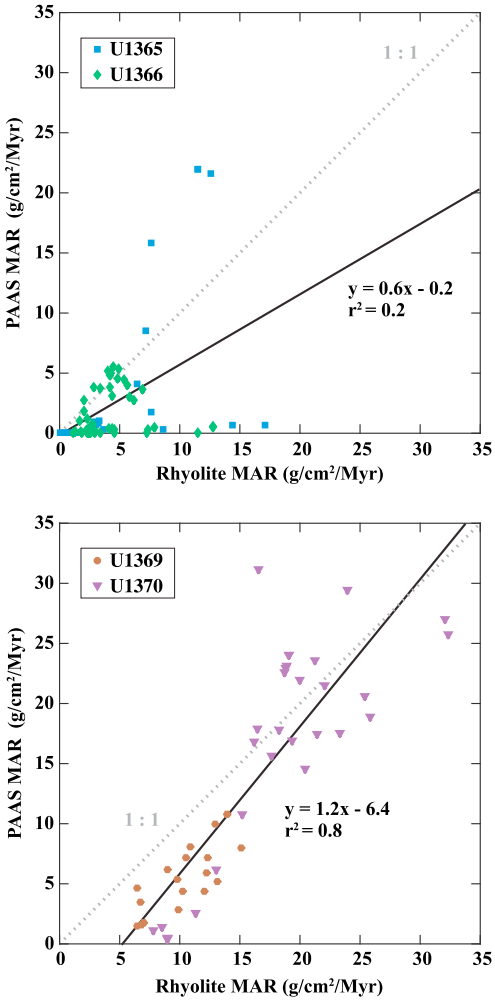

Figure 9. PAAS mass accumulation rate (g/cm^2/Myr) versus rhyolite mass accumulation rate (g/cm^2/Myr) at (top) Sites U1365 and U1366 and (bottom) Sites U1369 and U1370. The black line is a linear fit to all the points in each plot, and the equations and r^2 are expressed on the plot. One outlier with anomalously high rhyolite MAR (at 100 Ma) was removed from Site U1365 to ensure that samples older than 65 Ma were not biasing the correlation. The dotted gray line marks a 1:1 ratio for reference.

compare the MAR of PAAS and rhyolite (Figure 9) at the SPG sites and find that the extent of the correlation of dust and ash in our data depends on the latitude of the site. The more northern Sites U1365 and U1366 exhibit no significant covariance ($r^2 = 0.2$) between the MAR of PAAS and rhyolite (Figure 9, top). However, a significant positive correlation ($r^2 = 0.8$) between PAAS and rhyolite MAR is observed at the more southern Sites U1369 and U1370 (Figure 9, top). The different relationships at different sites reinforce our confidence that our Co-based accumulation rate methodology and statistical modeling have not systematically biased the MAR data toward a positive, negative, or any correlation between PAAS and rhyolite. Instead, its fidelity allows us to examine the latitudinal differences in processes that control the accumulation of PAAS and rhyolite in pelagic clay.

The accumulation of eolian dust and ash in marine sediment is the sum of four processes, including: (1) Production (dust availability and volcanic ash emission), (2) Transport (paleolocation and wind direction and/or intensity), (3) Deposition (settling through the water column to the seafloor), and (4) Preservation (chemical and physical). Since dust and ash in the pelagic clay have similar grain sizes and their general aluminosilicate nature [*Stancin et al.*, 2008; *Dubois et al.*, 2014], we expect that they behave broadly similarly in the deposition and preservation processes, at least to the extent relevant to this study. If this assumption is correct, then differences in production and/or transport must have caused the different PAAS and rhyolite accumulation rates at Sites U1365 and U1366.

Temporal differences in *production* would have depended on the timing of Australian aridification and the timing of episodes of volcanic activity. Also, the production of dust and ash may have differed spatially depending on the latitude at which Australia aridifies or where volcanism occurs.

Transport process may vary depending on the direction and strength of the prevailing winds in the troposphere or the stratosphere at the latitude of the site. Throughout the Cenozoic, Sites U1365 and U1366 migrated north across 30°S, possibly crossing into a different prevailing wind belt or into latitudes more sensitive to shifts in Hadley Cell circulation. Climate simulations demonstrate that the north-south position of the Intertropical Convergence Zone (ITCZ) and Hadley Cell responds to changes in interhemispheric temperature and ice sheet contrasts [e.g., *Broccoli et al.*, 2006]. This sensitivity has been documented in the geological past as well. For example, there is evidence of a northward shift in the ITCZ when ice sheets expanded on Antarctica in the mid-Miocene [*Holbourn et al.*, 2010]. Similarly, Northern Hemisphere ice growth starting in the late Miocene may have shifted Northern Hemisphere westerlies southward [*Chang et al.*, 2013]. The hemispheric asymmetries shift the whole Hadley Cell including the

downwelling arid air masses around 30°S. These shifts may have caused Sites U1365 and U1366 to experience variable prevailing wind directions even if the latitude of the site itself did not change. A northward shift (as we propose occurred in the mid-Miocene, ~15–10 Ma) would have kept the sites within the westerlies and downwind of Australia. This may partly explain the episode of rapid PAAS accumulation that occurred at these sites at this time. A southward shift (as we propose occurred in the late Miocene) would have caused the easterlies to be the prevailing wind direction over these sites at this time. The sites would not have been downwind of Australia, and deposition may have been limited to ash. Shifting wind belts may explain (i) the intervals of very low accumulation of PAAS at Site U1365 (also observed at Site 596) [*Zhou and Kyte*, 1992] after the mid-Miocene and (ii) why dust and ash do not covary at Sites U1365 and U1366.

For the MAR of dust and ash to behave similarly (as observed at the more southern Sites U1369 and U1370), both the production and transport of dust and ash must have been similar or one process must have dominated over the other. Unlike Sites U1365 and U1366, throughout the Cenozoic, Sites U1369 and U1370 have always been located between ~30 and 60°S within the prevailing westerlies. These sites were always downwind of the sources of Australia dust and New Zealand arc volcanism, which were at overlapping latitudes. The MAR of rhyolite relative to the MAR of PAAS at Site U1369 was broadly similar to that at Site U1370 (Figure 9, bottom), but the absolute MAR of both PAAS and rhyolite was generally higher at Site U1370. This finding indicates that both of these sites received a similar ratio of dust:ash abundance, but the site closer to Australia accumulated dust and ash more rapidly. These patterns collectively suggest that at least transport pathways were similar for both PAAS and volcanic ash.

8. Summary

We analyzed major, trace, and rare earth elements in 206 bulk sediment samples from seven sites in the South Pacific. We used multivariate statistical partitioning techniques to identify and quantify six sediment source components for these samples. These components are PAAS, rhyolite, altered basalt, Fe-Mn oxyhydroxide, apatite, and excess Si. By applying a Co-based age model to four of the sites dominated by pelagic clay, we assess the timing of changes in mass accumulation rate of each sediment source to characterize the spatial and temporal evolution of the South Pacific Gyre through the Cenozoic.

Fe-Mn oxyhydroxides accumulated most rapidly near the basement at each site and decreased rapidly as the site migrated away from the MOR. Sites U1365 and U1366 may have sustained higher hydrothermal MARs due to their proximity to the Osbourn Trough in the Cretaceous. The rapid deposition of Fe-Mn oxyhydroxides at Site U1366 decreased sharply at the same time that the Osbourn Trough is predicted to have ceased spreading.

Excess Si preserved in the sediment as frustules or Si-enriched authigenic phases accumulated rapidly at Sites U1365 and U1366 in the Late Cretaceous, suggesting the distribution of siliceous plankton production was different from modern day. Sites U1369 and U1370 experienced an increase in excess Si ~8 Ma when Site U1371 transitioned from pelagic clay to siliceous deposition, supporting hypotheses of a major reorganization of ocean nutrients distributions in the southern SPG at this time.

The accumulation of eolian dust and volcanic ash reflects spatial and temporal variations in the production and transport of both materials. Sites U1371 and U1370, which are closer to and downwind of Australia, have a stronger dust signature than the sites farther north and closer to the center of the SPG. Beginning in the early Eocene, the MAR of dust increased gradually with multiple sites experiencing local maxima at the Eocene-Oligocene boundary and the mid-Miocene. These multisite patterns record variations of the dust deposition in the open ocean during the aridification of Australia as it migrated into an arid belt at ~30°S, while cooling and aridification occurred globally.

Dispersed volcanic ash is a significant component of SPG pelagic clay, often comprising >50% of the bulk sediment by mass. Rhyolitic and basaltic ash accumulation gradually increased throughout the Cenozoic with episodes of increased accumulation at each site. At the more northern Sites U1365 and U1366, the dust MAR and ash MAR are not well correlated, suggesting a difference in production and/or transport processes at these more northern sites. One possible explanation is that asymmetrical interhemispheric temperature and ice growth caused meridional shifts in atmospheric circulation cells and the more northern sites to experience variable prevailing wind patterns. At the more southern Sites U1369 and

U1370, the dust MAR and ash MAR are significantly correlated, suggesting similar production and/or transport mechanisms. The sites have remained within the prevailing westerlies between ~30 and 60°S and downwind of Australia throughout the Cenozoic, which suggests that at least similar transport mechanisms may have influenced the relationship between dust and ash.

Acknowledgments

We thank S.A. Hovan and two anonymous reviewers for their detailed comments on the manuscript. We are particularly grateful to R.A. Pockalny for his advice and comments on various aspects of this project. We thank T. Ireland, J.W. Sparks, and R.P. Scudder at Boston University for their analytical assistance and many conversations. The help of C. Atta and M. Hulewicz in the lab is also greatly appreciated, and we also thank B.W. Hoppie and C. A. Alvarez Zarikian for their helpful discussions. This research used samples and data provided by the Integrated Ocean Drilling Program (IODP). Funding for this research was provided by the U.S. National Science Foundation to R.W.M. (NSF OCE1130531) as well as S.D. and A.J.S. (NSF OCE1130735). USSSP postcruise support was provided to Expedition 329 shipboard participants R.W.M., R.N.H., S.D., and A.J.S. Portions of this material are based upon work supported, while R.W.M. was serving at the National Science Foundation. The data generated during and used in this study are included in five tables in the supporting information files; any additional data may be obtained from A.G.D. (email: adunlea@bu.edu).

References

Alvarez Zarikian, C. A. (2015), Cenozoic bathyal and abyssal ostracods beneath the oligotrophic South Pacific Gyre (IODP Expedition 329 Sites U1367, U1368 and U1370), *Palaeogeogr. Palaeoclimatol. Palaeoecol.*, *419*, 115–142.

Barrett, T. J., P. N. Taylor, and J. Lugoqski (1987), Metalliferous sediments from DSDP Leg 92: The East Pacific Rise transect, *Geochim. Cosmochim. Acta*, *51*, 2241–2253.

Bijl, P. K., J. A. Bendle, S. M. Bohaty, J. Pross, S. Schouten, L. Tauxe, C. E. Stickley, R. M. McKay, U. Röhl, and M. Olney (2013), Eocene cooling linked to early flow across the Tasmanian Gateway, *Proc. Natl. Acad. Sci. U.S.A.*, *110*, 9645–9650.

Billen, M. I., and J. Stock (2000), Morphology and origin of the Osbourn Trough, *J. Geophys. Res.*, *105*, 13,481–13,489, doi:10.1029/2000JB900035.

Broccoli, A. J., K. A. Dahl, and R. J. Stouffer (2006), Response of the ITCZ to Northern Hemisphere cooling, *Geophys. Res. Lett.*, *33*, L01702, doi:10.1029/2005GL024546.

Carter, L., B. Alloway, P. Shane, and J. Westgate (2004), Deep-ocean record of major late Cenozoic rhyolitic eruptions from New Zealand, *N. Z. J. Geol. Geophys.*, *47*, 481–500.

Chang, H., Z. An, F. Wu, Z. Jin, W. Liu, and Y. Song (2013), A Rb/Sr record of the weathering response to environmental changes in westerly winds across the Tarim Basin in the late Miocene to early Pleistocene, *Palaeogeogr. Palaeoclimatol. Palaeoecol.*, *386*, 364–373.

Cortese, G., and C. A. Alvarez Zarikian, (2015). Data report: Radiolarian occurrences at IODP Expedition 329 Site U1371, in *Proceeding of the Integrated Ocean Drilling Program*, vol. 329, Integrated Ocean Drilling Program Management International, Inc., Tokyo, doi:10.2204/iodp.proc.329.2011, in press.

Cuadros, J., V. M. Dekov, X. Arroyo, and F. Nieto (2011), Smectite formation in submarine hydrothermal sediments: Samples from the HMS Challenger Expedition (1872–1876), *Clays Clay Miner.*, *59*, 147–164.

D'Hondt S., F. Inagaki, C. A. Alvarez Zarikian, and Expedition 329 Scientists (2011), Expedition 329 Reports, in *Proceedings of the Integrated Ocean Drilling Program*, vol. 329, Integrated Ocean Drilling Program Management International, Inc., Tokyo, doi:10.2204/iodp.proc.329.2011.

D'Hondt, S., et al. (2015), Presence of oxygen and aerobic communities from sea floor to basement in deep-sea sediments, *Nat. Geosci.*, *8*, 299–304.

Downey, N. J., J. M. Stock, R. W. Clayton, and S. C. Cande (2007), History of the Cretaceous Osbourn spreading center, *J. Geophys. Res.*, *112*, B04102, doi:10.1029/2006JB004550.

Dubois N., N. C. Mitchell, and I. R. Hall (2014) Data report: Particle size distribution for IODP Expedition 329 sites in the South Pacific Gyre, in *Proceedings of the Integrated Ocean Drilling Program*, vol. 329, Integrated Ocean Drilling Program Management International, Inc., Tokyo, doi:10.2204/iodp.proc.329.201.2014.

Dunlea, A. G., R. W. Murray, J. Sauvage, R. A. Pockalny, A. J. Spivack, S. D'Hondt, and R. N. Harris (2015), Cobalt-based age models of pelagic clay in the South Pacific Gyre, *Geochem. Geophys. Geosyst.*, doi:10.1002/2015GC005892.

Dymond, J., and W. Eklund (1978), A microprobe study of metalliferous sediment components, *Earth Planet. Sci. Lett.*, *40*, 243–251.

Dzaugis, M. E., A. J. Spivack, A. G. Dunlea, and R. W. Murray (2013), Radiolytic hydrogen production in basaltic basement of the South Pacific Gyre, Abstract B13C-0486 presented at 2013 Fall Meeting, AGU, San Francisco, Calif., 9–13 Dec.

Elderfield, H., and A. Schultz (1996), Mid-ocean ridge hydrothermal fluxes and the chemical composition of the ocean, *Annu. Rev. Earth Planet. Sci.*, *24*, 191–224.

Fitzsimmons, J. N., E. A. Boyle, and W. J. Jenkins (2014), Distal transport of dissolved hydrothermal iron in the deep South Pacific Ocean, *Proc. Natl. Acad. Sci. U.S.A.*, *111*, 16,654–16,661.

Gale, A., C. A. Dalton, C. H. Langmuir, Y. Su, and J.-G. Schilling (2013), The mean composition of ocean ridge basalts, *Geochem. Geophys. Geosyst.*, *14*, 489–518, doi:10.1029/2012GC004334.

Gardner, J. V., C. S. Nelson, and P. A. Baker (1986), Distribution and character of pale green laminae in sediment from Lord Howe Rise: A probable late Neogene and Quaternary tephrostratigraphic record, *Deep Sea Drill. Proj. Initial Rep.*, *90*, 1145–1159.

Gromet, L. P., R. F. Dymek, L. A. Haskin, and R. L. Korotev (1984), The "North American shale composite": Its compilation, major and trace element characteristics, *Geochim. Cosmochim. Acta*, *48*, 2469–2482.

Gurnis, M., M. Turner, S. Zahirovic, L. DiCaprio, S. Spasojevic, R. D. Müller, J. Boyden, M. Seton, V. C. Manea, and D. J. Bower (2012), Plate tectonic reconstructions with continuously closing plates, *C. R. Geosci.*, *38*, 35–42.

Holbourn, A., W. Kuhnt, M. Regenberg, M. Schulz, A. Mix, and N. Andersen (2010), Does Antarctic glaciation force migration of the tropical rain belt?, *Geology*, *38*, 783–786.

Kastner, M. (1999), Oceanic minerals: Their origin, nature of their environment and significance, *Proc. Natl. Acad. Sci. U.S.A.*, *96*, 3380–3387.

Kyte, F. T., M. Leinen, H. G. Ross, and L. Zhou (1993), Cenozoic sedimentation history of the central North Pacific: Inferences from the elemental geochemistry of core LL44-GPC3, *Geochim. Cosmochim. Acta*, *57*, 1719–1740.

Leinen, M. (1987), The origin of paleochemical signatures in North Pacific pelagic clays: Partitioning experiments, *Geochim. Cosmochim. Acta*, *51*, 305–319.

Li, F., P. Ginoux, and V. Ramaswamy (2008), Distribution, transport, and deposition of mineral dust in the Southern Ocean and Antarctica: Contribution of major sources, *J. Geophys. Res.*, *113*, D10207, doi:10.1029/2007JD009190.

Li, Y.-H., and J. E. Schoonmaker (2003), Chemical composition and mineralogy of marine sediments, *Treatise Geochem.*, *7*, 1–35.

Loucaides, S., P. Michalopoulos, M. Presti, E. Koning, T. Behrends, and P. Van Cappellen (2010), Seawater-mediated interactions between diatomaceous silica and terrigenous sediments: Results from long-term incubation experiments, *Chem. Geol.*, *270*, 68–79.

Lyle, M., K. Dadey, and J. Farrell (1995), The late Miocene (11–8 Ma) eastern Pacific carbonate crash: Evidence for reorganization of deep-water circulation by the closure of the Panama Gateway, *Proc. Ocean Drill. Program Sci. Results*, *138*, 821–838.

Lyle, M. W. (1986), Major element composition of Leg 92 sediments, *Initial Rep. Deep Sea Drill. Program*, *92*, 355–370.

Mackie, D. S., P. W. Boyd, G. H. McTainsh, N. W. Tindale, T. K. Westberry, and K. A. Hunter (2008), Biogeochemistry of iron in Australian dust: From eolian uplift to marine uptake, *Geochem. Geophys. Geosyst.*, *9*, Q03Q08, doi:10.1029/2007GC001813.

Marchig, V., and J. Erzinger (1986), Chemical composition of Pacific sediments near 20 S: Changes with increasing distance from the East Pacific Rise, *Initial Rep. Deep Sea Drill. Program*, *92*, 371–381.

Martin, H. A. (2006), Cenozoic climatic change and the development of the arid vegetation in Australia, *J. Arid Environ.*, *66*, 533–563.
Martinez, N. C., R. W. Murray, G. R. Dickens, and M. Kölling (2009), Discrimination of sources of terrigenous sediment deposited in the central Arctic Ocean through the Cenozoic, *Paleoceanography*, *24*, PA1210, doi:10.1029/2007PA001567.
Martinez, N. C., R. W. Murray, R. C. Thunel, L. C. Peterson, F. Muller-Karger, L. Lorenzoni, Y. Astor, and R. Varela (2010), Local and regional geochemical signatures of surface sediments from the Cariaco Basin and Orinoco Delta, Venezuela, *Geology*, *38*, 159–162.
Moore, C. M., et al. (2013), Processes and patterns of oceanic nutrient limitation, *Nat. Geosci.*, *6*, 701–710.
Murray, R., D. J. Miller, and K. Kryc (2000), Analysis of major and trace elements in rocks, sediments, and interstitial waters by inductively coupled plasma–atomic emission spectrometry (ICP-AES), *Ocean Drill. Program Tech. Note*, *29*, 1–27.
Noble, D. C., E. H. McKee, E. Farrar, and U. Petersen (1974), Episodic Cenozoic volcanism and tectonism in the Andes of Peru, *Earth Planet. Sci. Lett.*, *21*, 213–220.
Olgun, N., S. Duggen, P. L. Croot, P. Delmelle, H. Dietze, U. Schacht, N. Óskarsson, C. Siebe, A. Auer, and D. Garbe-Schönberg (2011), Surface ocean iron fertilization: The role of airborne volcanic ash from subduction zone and hot spot volcanoes and related iron fluxes into the Pacific Ocean, *Global Biogeochem. Cycles*, *25*, GB4001, doi:10.1029/2009GB003761.
Pälike, H., M. W. Lyle, H. Nishi, I. Raffi, A. Ridgwell, K. Gamage, A. Klaus, G. Acton, L. Anderson, and J. Backman (2012), A Cenozoic record of the equatorial Pacific carbonate compensation depth, *Nature*, *488*, 609–614.
Passchier, S., S. M. Bohaty, F. Jiménez-Espejo, J. Pross, U. Rohl, T. van de Flierdt, C. Escutia, and H. Brinkhuis (2013), Early Eocene to middle Miocene cooling and aridification of East Antarctica, *Geochem. Geophys. Geosyst.*, *14*, 1399–1410, doi:10.1002/ggge.20106.
Peters, J. L., R. W. Murray, J. W. Sparks, and D. S. Coleman (2000), Terrigenous matter and dispersed ash in sediment from the Caribbean Sea: Results from Leg 165, *Proc. Ocean Drill. Program, Sci. Results*, *165*, 115–124.
Pisias, N. G., R. W. Murray, and R. P. Scudder (2013), Multivariate statistical analysis and partitioning of sedimentary geochemical data sets: General principles and specific MATLAB scripts, *Geochem. Geophys. Geosyst.*, *5*, 1–6, doi:10.1002/ggge.20247.
Plank, T., and C. H. Langmuir (1998), The chemical composition of subducting sediment and its consequences for the crust and mantle, *Chem. Geol.*, *145*, 325–394.
Ragueneau, O., P. Treguer, A. Leynaert, R. Anderson, M. Brzezinski, D. DeMaster, R. Dugdale, J. Dymond, G. Fischer, and R. Francois (2000), A review of the Si cycle in the modern ocean: Recent progress and missing gaps in the application of biogenic opal as a paleoproductivity proxy, *Global Planet. Change*, *26*, 317–365.
Rea, D. K., et al. (2006), Broad region of no sediment in the southwest Pacific Basin, *Geology*, *34*, 873–876.
Reimann, C., P. Filzmoser, and R. Garrett (2002), Factor analysis applied to regional geochemical data: Problems and possibilities, *Appl. Geochem.*, *17*, 185–206.
Rudnick, R. L., and S. Gao (2003), Composition of the continental crust, *Treatise Geochem.*, *3*, 1–64.
Ruhlin, D., and R. Owen (1986), The rare earth element geochemistry of hydrothermal sediments from the East Pacific Rise: Examination of a seawater scavenging mechanism, *Geochim. Cosmochim. Acta*, *50*, 393–400.
Saito, M. A., A. E. Noble, A. Tagliabue, T. J. Goepfert, C. H. Lamborg, and W. J. Jenkins (2013), Slow-spreading submarine ridges in the South Atlantic as a significant oceanic iron source, *Nat. Geosci.*, *6*, 775–779.
Scudder, R. P., R. W. Murray, and T. Plank (2009), Dispersed ash in deeply buried sediment from the northwest Pacific Ocean: An example from the Izu–Bonin arc (ODP Site 1149), *Earth Planet. Sci. Lett.*, *284*, 639–648.
Scudder, R. P., R. W. Murray, J. C. Schindlbeck, S. Kutterolf, F. Hauff, and C. C. McKinley (2014), Regional-scale input of dispersed and discrete volcanic ash to the Izu-Bonin and Mariana subduction zones, *Geochem. Geophys. Geosyst.*, *15*, 4369–4379, doi:10.1002/2014GC005561.
Seton, M., et al. (2012), Global continental and ocean basin reconstructions since 200 Ma, *Earth Sci. Rev.*, *113*, 212–270.
Stancin, A. M., J. D. Gleason, S. A. Hovan, D. K. Rea, R. M. Owen, T. C. Moore Jr., C. M. Hall, and J. D. Blum (2008), Miocene to recent eolian dust record from the Southwest Pacific Ocean at 40°S latitude, *Palaeogeogr. Palaeoclimatol. Palaeoecol.*, *261*, 218–233.
Stein, R., and C. Robert (1986), Siliciclastic sediments at Sites 588, 590, and 591—Neogene and Paleogene evolution in the southwest Pacific and Australian climate, *Initial Rep. Deep Sea Drill. Program*, *90*, 1437–1455.
Straub, S. M., and H. U. Schmincke (1998), Evaluating the tephra input into Pacific Ocean sediments: Distribution in space and time, *Geol. Rundsch.*, *87*, 461–476.
Suto, I., and G. Uramoto (2015), Data report: Diatom biostratigraphy of IODP Expedition 329 Site U1371 in the South Pacific Ocean, in *Proceeding of the Integrated Ocean Drilling Program*, vol. 329, Integrated Ocean Drilling Program Management International, Inc, Tokyo in press.
Takebe, M. (2005), Carriers of rare earth elements in Pacific deep-sea sediments, *J. Geol.*, *113*, 201–215.
Taylor, S. R., and S. M. McLennan (1985), *The Continental Crust: Its Composition and Evolution*, 312 pp., Blackwell Sci., Oxford, U. K.
Taylor, S. R., S. M. McLennan, and M. T. McCulloch (1983), Geochemistry of loess, continental crustal composition and crustal model ages, *Geochim. Cosmochim. Acta*, *47*, 1897–1905.
Wheat, C. G., R. A. Feely, and M. J. Mottl (1996), Phosphate removal by oceanic hydrothermal processes: An update of the phosphorus budget in the oceans, *Geochim. Cosmochim. Acta*, *60*, 3593–3608.
Willbold, M., and A. Stracke (2006), Trace element composition of mantle end-members: Implications for recycling of oceanic and upper and lower continental crust, *Geochem. Geophys. Geosyst.*, *7*, Q04004, doi:10.1029/2005GC001005.
Yamamoto, K., R. Sugisaki, and F. Arai (1986), Chemical aspects of alteration of acidic tuffs and their application to siliceous deposits, *Chem. Geol.*, *55*, 61–76.
Zachos, J., M. Pagani, L. Sloan, E. Thomas, and K. Billups (2001), Trends, rhythms, and aberrations in global climate 65 Ma to present, *Science*, *292*, 686–693.
Zhang, G.-L., and C. Smith-Duque (2014), Seafloor basalt alteration and chemical change in the ultra thinly sedimented South Pacific, *Geochem. Geophys. Geosyst.*, *15*, 3066–3080, doi:10.1002/2013GC005141.
Zhou, L., and F. T. Kyte (1992), Sedimentation history of the South Pacific pelagic clay province over the last 85 million years inferred from the geochemistry of Deep Sea Drilling Project Hole 596, *Paleoceanography*, *7*, 441–465, doi:10.1029/92PA01063.
Ziegler, C. L., and R. W. Murray (2007), Geochemical evolution of the central Pacific Ocean over the past 56 Myr, *Paleoceanography*, *22*, PA2203, doi:10.1029/2006PA001321.
Ziegler, C. L., R. W. Murray, S. A. Hovan, and D. K. Rea (2007), Resolving eolian, volcanogenic, and authigenic components in pelagic sediment from the Pacific Ocean, *Earth Planet. Sci. Lett.*, *254*, 416–432.
Ziegler, C. L., R. W. Murray, T. Plank, and S. R. Hemming (2008), Sources of Fe to the equatorial Pacific Ocean from the Holocene to Miocene, *Earth Planet. Sci. Lett.*, *270*, 258–270.